universität wien

MASTERARBEIT / MASTER'S THESIS

Titel der Masterarbeit / Title of the Master's Thesis

„Characterisation of condensation particle counters for airborne measurements"

verfasst von / submitted by

Dorian Spät, BSc

angestrebter akademischer Grad / in partial fulfilment of the requirements for the degree of

Master of Science (MSc)

Wien, 2020 / Vienna, 2020

Acknowledgements

Abstract

Condensation particle counters (CPCs) are the most common instruments used to measure number concentrations of aerosol particles. They are especially important regarding the size range below 100 nm, which may also be a field of interest at airborne measurement campaigns. Aircraft based experiments however, require the deployed devices to have the ability to maintain performance over a wide span of ambient temperature and pressure (e.g. down to 100-200 hPa). The latter is particularly challenging concerning CPCs and although many studies focused on characterizations of these instruments, only a limited number investigated their performance under low pressure conditions. Therefore, the aim of this thesis is to characterize two TSI 3772-CEN CPCs at low pressure conditions, in order to achieve a better understanding of the CPCs behaviour in airborne applications and improve the data interpretation. To do so, detection efficiency and volumetric flow rate measurements at various pressure settings between 1000 and 150 hPa were performed with both TSI 3772-CEN CPCs, under controlled laboratory conditions. Different seed particle species (Ag, NaCl and $C_{15}H_{24}O_x$) and diameters (ranging from 7 to 100 nm) were investigated. At low pressures, the CPCs were operated without the working fluid supply bottles, to avoid flooding of the instruments with n-butanol. A strong decrease in detection efficiency below about 350 hPa was observed, which is in agreement with literature. Below 250 hPa, small differences in detection efficiencies were found between the two TSI 3772-CEN devices. In addition, a theoretical assessment was conducted, in an attempt to explain experimental data. At low pressure conditions a clear difference between the measurements and the simulation results was found. In the theoretical data, a drop similar to the experimental results can only be seen to some extent at pressures below 150 hPa. Further deliberations are necessary for a complete description of the processes taking place inside the TSI 3772-CEN CPCs at low pressure. The findings of this study can support the decision making process to assess whether the application of TSI 3772-CEN CPCs at individual aircraft campaigns is reasonable or not, depending on planned elevations.

Zusammenfassung

Kondensationspartikelzähler (CPCs) sind die am häufigsten verwendeten Instrumente zur Messung der Anzahlkonzentrationen von Aerosolpartikeln. Sie sind besonders wichtig im Hinblick auf den Größenbereich unter 100 nm, der auch bei luftgetragenen Messkampagnen von Interesse sein kann. Flugzeuggestützte Experimente erfordern jedoch, dass die eingesetzten Geräte in der Lage sind, ihre Leistung über einen weiten Bereich von Umgebungstemperatur und -druck aufrechtzuerhalten (z.B. bis hinunter zu 100-200 hPa). Letzteres ist bei CPCs eine besondere Herausforderung und obwohl sich viele Studien auf die Charakterisierung dieser Instrumente konzentrierten, untersuchte nur eine begrenzte Anzahl ihre Leistung unter Niederdruckbedingungen. Das Ziel dieser Arbeit ist es daher, zwei TSI 3772-CEN CPCs unter Niederdruckbedingungen zu charakterisieren, um ein besseres Verständnis des Verhaltens der CPCs in flugzeuggestützten Anwendungen zu erreichen und die Interpretation der Daten zu verbessern. Zu diesem Zweck wurden Messungen der Detektionseffizienz und der volumetrischen Durchflussrate bei verschiedenen Druckeinstellungen zwischen 1000 und 150 hPa mit den beiden TSI 3772-CEN CPCs unter kontrollierten Laborbedingungen durchgeführt. Verschiedene Partikelarten (Ag, NaCl und $C_{15}H_{24}O_x$) und Durchmesser (im Bereich von 7 bis 100 nm) wurden untersucht. Bei niedrigen Drücken wurden die CPCs ohne die Versorgungsflaschen für die Arbeitsflüssigkeit betrieben, um eine Überflutung der Instrumente mit n-Butanol zu vermeiden. Es wurde eine starke Abnahme der Detektionseffizienz unter etwa 350 hPa beobachtet, was mit der Literatur übereinstimmt. Unterhalb von 250 hPa wurden kleine Unterschiede in den Detektionseffizienzen zwischen den beiden TSI 3772-CEN Geräten festgestellt. Zusätzlich wurde eine theoretische Bewertung durchgeführt, um die experimentellen Daten zu erklären. Bei niedrigen Druckbedingungen wurde ein deutlicher Unterschied zwischen den Messungen und den Simulationsergebnissen festgestellt. In den theoretischen Daten ist ein, den experimentellen Ergebnissen ähnlicher Abfall, bei Drücken unter 150 hPa nur bis zu einem gewissen Grad zu erkennen. Für eine vollständige Beschreibung der Prozesse, die in den TSI 3772-CEN CPCs bei niedrigem Druck ablaufen, sind weitere Überlegungen erforderlich. Die Ergebnisse dieser Studie können den Entscheidungsfindungsprozess unterstützen, um zu beurteilen, ob der Einsatz von TSI 3772-CEN CPCs bei einzelnen Flugzeugkampagnen, in Abhängigkeit von den geplanten Flughöhen sinnvoll ist oder nicht.

Contents

Acronyms

K_R	Kelvin Ratio
S_R	Saturation Ratio
S_S	Supersaturation
BCy	Beta Caryophyllene
CCN	Cloud Condensation Nuclei
CPC	Condensation Particle Counter
DMA	Differential Mobility Analyzer
FCE	Faraday Cup Electrometer
IN	Ice Nuclei
IPCC	Intergovernmental Panel on Climate Change
MFM	Mass Flow Meter
NMASS	Nucleations Mode Aerosol Size Spectrometer
OPC	Optical Particle Counter
PDE	Partial Differential Equation
SOA	Secondary Organic Aerosol

Glossary

$(NH_4)_2SO_2$	chemical compound Ammonium Sulfite
Ag	chemical element Silver
$C_{15}H_{24}O_x$	natural sesquiterpene Beta Caryophyllene
NaCl	ionic compound Sodium chloride
O_3	inorganic molecule Ozone consisting of three oxygen atoms

1 Introduction

Atmospheric Aerosols and their Importance

The Earth's atmosphere does not solitary consist of air, but also of liquid and solid particles dispersed in it (Hinds, 1999). The investigation of such two phased systems, containing particles suspended in a carrier gas, is the domain of aerosol physics. These aerosol particles can be differentiated in primary and secondary types, depending on their formation. Whereat the former are directly emitted into the atmosphere (such as sea salt or mineral dust) and the latter evolve there (form from vapors i.e. gas-to-particle conversion) (Hinds, 1999). Its origin can be either natural or anthropogenic. Furthermore, particles in the air may undergo various processes such as growth or change in composition (e.g due to condensation or coagulation). Depending on their size and composition, aerosol may have various impacts on weather and climate, by influencing the Earth's radiation budget. The effects range from direct interactions with the incoming solar radiation via scattering and absorption, to numerous indirect influences. The particles can provide sites for heterogenous reactions (Ravishankara, 1997), or serve as cloud condensation nuclei (CCN) and ice nuclei (IN), which impact the formation of cloud droplets and ice crystals. Therefore also the resulting clouds and thereby cloud albedo, as well as their lifetime depend on the properties and concentrations of the CCN and IN. Due to this wide spectrum of interactions both, cooling and warming effects can be the consequences arising from airborne particles, depending on their size, shape, composition, and so forth. The uncertainties, respective these effects, however and their spatiotemporal distribution of aerosol particles are still large (IPCC, 2013).

One way to tackle the gaps of knowledge regarding atmospheric aerosol particles and reduce the respective uncertainties, is to carry out measurements at locations and altitudes not yet well explored, such as mid and upper troposphere. Aircraft campaigns can cover wide areas of the atmosphere, which are inaccessible otherwise. However, while many instruments are well established for ground based measurements, the challenging environmental conditions of aircraft-based sampling of aerosol properties still demand further effort in terms of instrument calibration, modification or development. For instance, there is a limited number of instruments at the moment that can reliably measure particle number concentration in an environment where altitude, pressure and temperature may change rapidly, and that could be exposed to a wide range of operating pressures.

Particle number concentration is one of the fundamental parameters used to characterize aerosol, aerosol chemical processes, their optical properties or particle microphysics in the atmosphere (Takegawa and Sakurai, 2011). The size dependent distribution of these particles usually covers multiple orders of magnitude, from about 1 nm to 50 um in diameter D_p.

Atmospheric Aerosol Measurement

Condensation particle counters (CPCs) are the most common instruments used to measure particle number concentrations. They are especially important for the detection of particles in the ultra-fine modes (nucleation (D_p smaller than 20 nm) and Aitken mode (D_p between 20 nm and $\sim$ 100 nm)), since the lower detection limit of optical measurement systems typically matches the upper limit of Aitken mode (Hinds, 1999). Currently, there are four main types of CPCs in use, including expansion type, mixing type, diffusion type, and conductive cooling type (McMurry, 2000).

The first expansion type CPC was developed by Aitken already in 1888. It was called "dust counter" and for the first time it overcame the restrictions of optical detection (McMurry, 2000). Such instruments are drafted with water as working fluid and consist of a humidifier, an expansion chamber and a detector. These CPCs operate with a cyclic flow, thus a comparison to other instruments is not possible (Kulkarni et al., 2011).
Different types of CPCs were developed since, solving this problem. By mixing HCl vapor with saturated water vapor and aerosol, Holl and Mühleisen (1955) created a steady state CPC, driven by multicomponent condensation, since the mixture is supersaturated. Later on, Kousaka et al. (1982) and Vanhanen et al. (2011) redefined the mixing type CPC, utilizing different mechanisms to achieve supersaturation.
Another type of CPC is the differential diffusion type. Like the Aitken type, water acts as working fluid, but a continuous flow permits a bigger range of applications. Hoppel et al. (1979) first published the design of such a segmented thermal diffusion chamber.
Today the most commonly used version of CPCs is the conductive cooling type, originally developed by Rosen et al. (1974), Sinclair and Hoopes (1975) and Bricard et al. (1976) respectively. The first commercial instrument was the TSI 3020 designed by Agarwal and Sem (1980). Alcohol (such as n-butanol, or isoprpanol) is utilized as working fluid. The continuous aerosol stream first passes a saturator, which is kept at an elevated temperature, so that the stream afterwards is saturated with the working fluid. Next the aerosol is induced to a condenser tube, which is maintained at a lower temperature. Since the stream is cooled faster, than the alcohol vapor concentration depletes, supersaturation occurs. Subsequently an optical detection system measures the number concentration (Kulkarni et al., 2011).

Modern CPCs enable number concentration measurements of aerosol particles with diameters in the low single digit nm range (e.g. TSI 3756, TSI 3788, all Grimm models) . This lower detection limit is defined by the cut-off diameter, which is the particle diameter D_{50}, at which the counting efficiency of the CPC reaches 50 % (i.e. 50 % of the incoming particles are detected) with respect

to a reference instrument (Zhang and Liu, 1990; Kesten et al., 1991). The corresponding value of D_{50} depends on the CPC model and its structure and is mainly caused by diffusion losses (Kulkarni et al., 2011). Various approaches have been made to lower this limit (e.g. Kulkarni et al., 2011 and sources within), such as developing new instruments (e.g. Vanhanen et al., 2011; Hering et al., 2017) or varying temperatures within established CPCs (e.g. Kuang et al., 2012; Kangasluoma et al., 2015; Tauber, Steiner and Winkler, 2019).

Aircraft Application of CPCs

A number of aircraft based campaigns such as Jonsson et al. (1996), STREAM II (Schröder and Ström, 1997), SALTRACE (Weinzierl et al., 2017), ACRIDICON-CHUVA (e.g. AMETHYST in Andreae et al. (2018)), or ATom (e.g. NMASS in Williamson et al. (2018)) utilized CPCs or CPC-based systems on board of aircrafts. In many of these studies a combination of CPCs with optical particle counters (OPCs) was utilized. Measurements for size distribution information on aircraft, provide a critical insight into aerosol processes and have lead to major advances in the knowledge on new particle formation and growth processes, their properties or locations of their occurrence.

The low detection limit in combination with other advantages of CPCs, such as fast response time, the ability to measure very low number concentrations and their low maintenance needs, make them desired for airborne measurements. The latter, however, requires instruments to be suitable to operate in a large range of ambient pressures (e.g. down to 150-200 hPa), rapid changes in altitude and temperature. Although many studies focused on characterisations of conductive cooling type CPCs (e.g. Wiedensohlet et al. (1997); Kupc et al. (2013)), only a limited number investigated their performance under low pressure conditions (such as Zhang and Liu (1990, 1991); Hermann and Wiedensohler (2001); Takegawa and Sakurai (2011)). It was found that the counting efficiency of a CPC is pressure dependent.

- One of the first surveys done in this area, is a theoretical study, which has been carried out by Zhang and Liu (1990). This study investigated the performance of a TSI 3020 CPC dependent on pressure, flow rate and temperature of saturator and condenser. By solving the heat and mass transfer equations, for the conditions in the condenser, they were able to determine a single factor correlating with the counting efficiency. This factor combines the effects due to flow, pressure and structure of the condenser-tube. Their calculations show a cutoff-shift to larger particle sizes with decreasing pressure.

- Zhang and Liu (1991) subsequently performed laboratory experiments with the TSI 3760 CPC and NaCl particles at reduced pressures (down to 100 hPa) and found that the measured counting efficiency is in reasonably good

agreement with the theoretical results (shift to larger particles with decreasing pressure). Except at pressures below 0.2 atm, where they report large deviations to their previous study (the maximum counting efficiency reaches only about 1/8 of the value derived via the simulations).

- Hermann and Wiedensohler (2001) tested a TSI 7610 at low pressures, down to 160 hPa with silver particles. With decreasing pressure, they found a decrease of the asymptotic maximum counting efficiency (i.e. the maximum counting value achieved at a certain pressure, in comparison to the maximum at 1013 hPa), which is consistent with Zhang and Liu (1990,1991), but a shift to smaller particles, leading to opposite results with respect to Zhang and Liu (1990,1991).

- Takegawa and Sakurai (2011) performed very similar evaluations with a TSI 3771 CPC and sucrose (or propane flame soot) particles. In compliance with Zhang and Liu (1990,1991) and unlike Hermann and Wiedensohler (2001) they reported a shift to larger particle sizes with decreasing pressure. Concerning the maximum asymptotic counting efficiency, Takegawa and Sakurai confirm the previously described behaviour.

To avoid the issue of changing counting efficiencies with pressure, a different approach for airborne measurements using CPCs was described by Williamson et al. (2018). The nucleation mode aerosol size spectrometer (NMASS) consists of a battery of five CPCs running in parallel and provides size selected aerosol concentration measurements. By maintaining constant internal pressure of 120 hPa (below the expected ambient pressure), the NMASS operates reliably over a wide range of ambient pressures. A disadvantage is, that the orifice used to maintain the constant pressure causes significant particle losses at larger particle sizes (50 % counting efficiency at about 500 nm), so in operation an optical particle counter (OPC) was used to cover the exceeding size range.

Aim and Scope of the Thesis

The overall aim of this work was to characterise the performance of two TSI 3772-CEN conductive cooling CPCs at a range of operating pressure conditions down to 150 hPa, in order to achieve a better understanding of the instruments behaviour in airborne applications and improve the data interpretation. This is expected to improve the ability of measuring the number concentration of newly formed particles when installed on board of aircraft. In this thesis, two TSI 3772-CEN CPCs have been used to study the effects of pressure variations. This CPC model can possibly be used for airborne measurements, however has not yet been characterized for that specific usage. Experimental results were compared to literature and theoretical evaluations of the CPC's detection efficiency.

Thesis Structure
– Outlook on the following Chapters

A brief overview on aerosol distributions, as well as condensation theory is given in 2, covering the fundamental processes utilized by CPCs. Furthermore, particle transport mechanisms and electrical properties of aerosol particles are discussed. Section 3 provides information on the experimental and theoretical methods applied in this thesis, including explanatory notes on used instruments, setups, data evaluation and simulations carried out. In section 4, results of the conducted laboratory measurements and theoretical evaluations are presented and discussed. The final section 5 draws a conclusion on the thesis, including recommendations on the application of CPCs in aircraft.

2 Theory

In this chapter, a mathematical description of aerosol size distributions is provided, punctuating the importance of CPCs for ambient aerosol measurements. Followed by condensation theory, enabling the description of the processes undergoing in CPCs. Meaning, that the principle of how nano-particles can grow to an optically detectable size is outlined. Furthermore, particle transport loss mechanisms are discussed, which can reduce the counting efficiency of aerosol measuring devices. Finally, a short overview of the electrical properties of aerosol particles is given, which play an important role in particle size selection and detection. The information presented in this chapter is mainly based on explanations found in Hinds (1999), as well as in Seinfeld and Pandis (2006).

2.1 Aerosol particle size distributions

Precise statistical considerations concerning atmospheric aerosol particle size distributions are important, since the diameter of an airborne particle determines its lifetime as well as its physical properties and thereby possible effects on climate and human health. Such a size dependent aerosol particle distribution usually covers multiple orders of magnitude, which is why it is classified in a number of modes, such as nucleation mode with diameter D_p smaller than ~ 20 nm, Aitken mode (D_p between ~ 20 nm and ~ 100 nm), accumulation mode ($D_p \sim 0.1$ to ~ 2 μm) and coarse mode with sizes ranging from $D_p \sim 2$ μm to ~ 50 μm. In conjunction with these modes, a distinction into two mainly essential distributions can be made.

- **Number distribution $f_N(D_p)$:**

$$f_N(D_p) = \frac{dN}{dD_p}. \tag{2.1}$$

  With the number concentration of aerosol particles N.

- **Mass distribution $f_M(D_p)$:**

$$f_M(D_p) = \rho_p \cdot f_V(D_p) = \rho_p \cdot \frac{\pi}{6} D_p^3 \cdot f_N(D_p). \tag{2.2}$$

  With the particle's density ρ_p and the volume distribution $f_V(D_p)$.

While accumulation mode and coarse mode usually dominate the mass distribution (and thereby volume distribution), the ambient aerosol particle number concentration is usually dominated by the two finest modes (see section 1), as displayed in Figure 2.1. Elements of this domain are also referred to as ultra-fine particles, which consist of both formation types, mentioned earlier. Particles of the nucleation mode are usually of secondary nature, created by nucleation from the gas phase (like sulfate, nitrate or secondary organic aeosols). Most Aitken mode nuclei have a primary source (like sea salt, smoke, or combustion particles) and they often provide a site for condensation of secondary material.
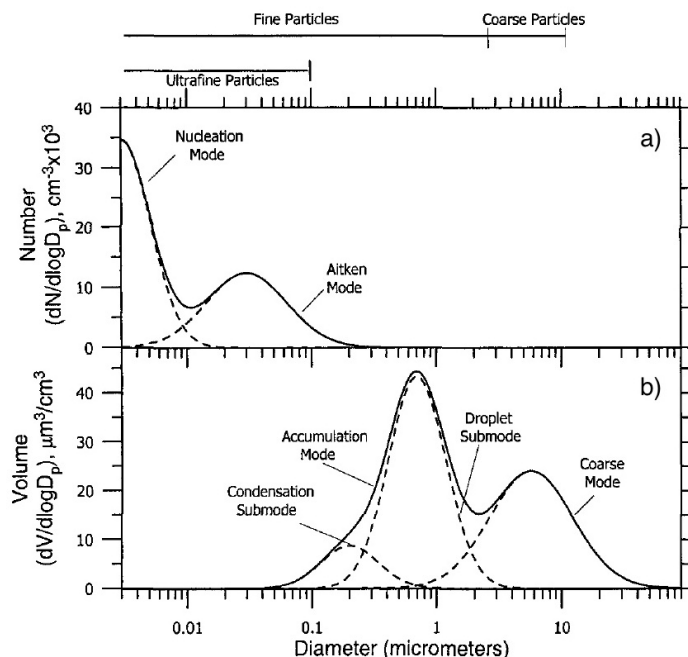
Figure 2.1: Presentation of aerosol size modes on the basis of typical distributions of atmospheric particles. Representation in terms of: a) number concentration b) mass concentration (Seinfeld and Pandis, 2006).

As already mentioned before, CPCs play an important role in the course of measuring aerosol particle size distributions, covering the ultra fine size range below 100 nm.

2.2 Condensation Theory

Condensation, i.e. the mass transfer process from gaseous to particulate phase, is an important mechanism for aerosol particle formation and growth in the atmosphere (Hinds, 1999). CPCs utilize this effect to grow existing aerosol particles, so that these are detectable by optical instrumentation (Kulkarni et al., 2011). It is a combination of two mechanisms. First nucleated condensation (or heterogeneous nucleation) and subsequently condensational growth, similar to processes taking place in nature (Hinds, 1999).

2.2.1 Nucleation

Two processes can lead to the formation of liquid droplets in a carrier gas. Homogeneous nucleation, which takes place without any additional particles and heterogeneous nucleation, which depends on the presence of aerosol particles and is utilized by CPCs. In general both of these forming mechanisms require supersaturated vapor of a condensable gas species. This supersaturation S_S is

defined via the **saturation ratio S_R**:

$$S_R = \frac{p_v}{p_S(T)}. \tag{2.3}$$

Where p_S is the saturation vapor pressure for a plane liquid surface, i.e. the pressure required to maintain a mass equilibrium between vapor and condensed vapor at a given temperature T. Whereat p_S rises with increasing T. The second pressure term in Equation 2.3, p_v is the actual partial pressure of the vapor. If this fraction exceeds one, so if $p_v > p_S(T)$ the observed vapor is supersaturated.

For the thermodynamical description of nucleation processes in a system with k chemical compounds, Volume V and entropy S, a useful quantity is the Gibbs free energy G.

$$G = U + pV - TS = \sum_{i=1}^{k} \mu_i n_i, \tag{2.4}$$

which leads to the *Gibbs-Dunham relation*, showing that with a change of the temperature T and the pressure p of the considered system, the chemical potentials μ_i of the compounds change correspondingly:

$$-SdT + Vdp = \sum_{i=1}^{k} n_i d\mu_i. \tag{2.5}$$

In the following subsections the two types of nucleation processes are described more precisely. First classical theory of homogeneous nucleation and thereafter heterogeneous nucleation.

2.2.2 Homogeneous Nucleation

The mathematically simplest considerable case of a nucleation process is taking place at conditions where there is just vapor of a single chemical species A. The curved interface of the emerging droplet has an effect on the amount of energy needed to form it. This energy value can be obtained via the Gibbs free energy,

$$\begin{aligned} \Delta G_{hom} &= G_{droplet} - G_{vapor} \\ &= -\frac{4\pi}{3} \frac{k_B T}{v_l} \cdot \ln{(S_R)} R_d^3 + 4\pi\sigma R_d^2. \end{aligned} \tag{2.6}$$

With the Boltzmann constant k_B, the volume v_l of a molecule of species A, the radius of the formed droplet R_d, and the surface tension σ.

Two cases can be distinguished, $S_R < 1$ and $S_R > 1$. The former results in a monotonically increasing ΔG_{hom} with R_d, since both terms in Equation 2.6 are positive. If $S_R > 1$, the first term of Equation 2.6, which is now negative, becomes more and more dominant with rising R_d, so that ΔG_{hom} decreases after reaching a maximum value ΔG_{hom}^* at R_d^*.
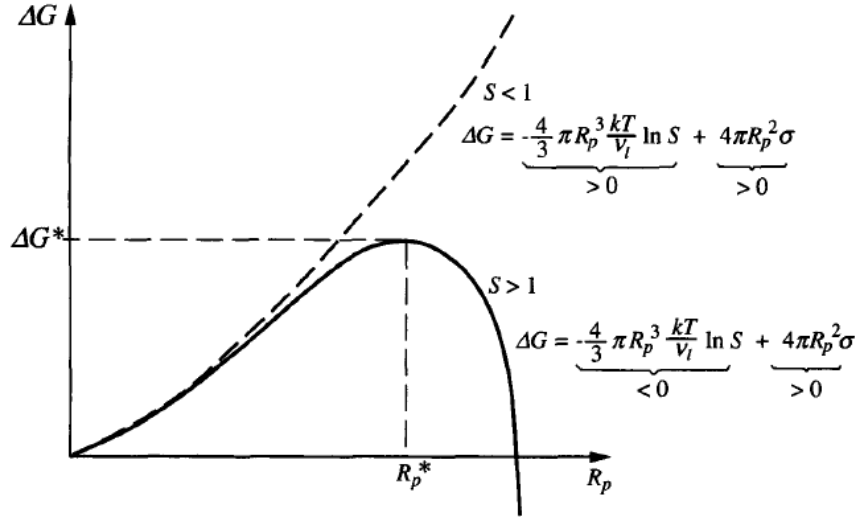
Figure 2.2: Energy required ($\Delta G = \Delta G_{hom}$) for formation of a droplet with radius R_d, where $S = S_R$ and $R_p = R_d$ (Seinfeld and Pandis, 2006).

By setting the first derivative of Equation 2.6, with respect to R_d to 0, the **Kelvin radius R_d^*** can be obtained:

$$R_d^* = \frac{2\sigma v_l}{k_B T \ln{(S_R)}}.$$

(2.7)

Inserting Equation 2.3, replacing R_d with $D_d = 2R_d$ and rearrangement yields to the **Kelvin** or **Thomas-Gibbs equation**:

$$
\begin{aligned}
S_R(D_d^*) = K_R = \frac{p_d}{p_S} &= exp\left(\frac{4\sigma v_l}{k_B T D_d^*}\right) \\
&= exp\left(\frac{4\sigma M}{\rho_l R T D_d^*}\right).
\end{aligned}
$$

(2.8)

The Kelvin ratio K_R specifies the relationship between the saturation S_R required for equilibrium and the droplet diameter D_d. With the surface tension σ, molecular weight M, density ρ_l of the droplet and the vapor pressure p_d at its surface. A droplet with the size of the *Kelvin diameter* D_d^* is at a metastable equilibrium, it will neither grow, nor evaporate. For homogeneous nucleation to occur, a liquid particle must initially reach the Kelvin diameter and condensationally grow subsequently. Experiments have shown, that molecule clusters are the origin of this process, not single molecules, which would require way higher supersaturations ($S_R = 220$ for water). These clusters already continuously form at unsaturated vapor, by reason of attractive forces (like Van der Waals forces), but disintegrate due to instability. When the saturation rises, their number concentration increases likewise and the probability of clusters reaching D_d^* grows.

2.2.3 Heterogeneous Nucleation

When nucleation occurs heterogeneously on an aerosol particle, the amount of new surface that needs to be created is smaller and so the free energy barrier is lower than for homogeneous nucleation. Additionally to the chemical species A from subsubsection 2.2.2, providing the vapor, now the presence of spherical particles also needs to be considered, complicating the process of droplet formation:

$$
\begin{aligned}
\Delta G^* &= \Delta G^*_{hom} \cdot f(m, x) \\
&= \frac{16\pi}{3} \frac{v_l^2 \sigma_{ev}^3}{(k_B T \ln(S_R))^2} \cdot f(m, x),
\end{aligned}
\tag{2.9}
$$

$$
D_d^* = \frac{4 v_l \sigma_{ev}}{k_B \ln S_R}.
\tag{2.10}
$$

Equation 2.9 describes the required energy for an embryo with critical diameter D_d^* (Equation 2.10 corresponding to Equation 2.7) to form on a preexisting particle via clustering, according to Fletcher (1958). Where σ_{ev} is the surface tension between embryo and surrounding (a high surface tension σ_{ev} results in a high value for the critical diameter). The function $f(m, x)$ takes the geometry of the embryo into account:

$$
\begin{aligned}
f(m, x) =& 1 + \left(\frac{1 - mx}{g}\right) + x^3 \left[2 - \left(\frac{x - m}{g}\right) + \left(\frac{x - m}{g}\right)^3\right] \\
&+ 3mx^2 \left(\frac{x - m}{g} - 1\right),
\end{aligned}
\tag{2.11}
$$

with

$$
g = (1 + x^2 - 2mx)^{1/2}.
\tag{2.12}
$$

Where $x = \frac{D}{D_d^*}$ and m is described by **Young's equation**, with the interfacial tensions between particle and surrounding σ_{pv}, as well as between particle and embryo σ_{pe}:

$$
m = \cos\theta = \frac{\sigma_{pv} - \sigma_{pe}}{\sigma_{ev}}.
\tag{2.13}
$$

The contact angle θ between embryo and pre-existing particle is an important parameter for heterogeneous nucleation. A schematic of the situation is presented in 2.3. For small angles, the corresponding particle diameter is big and conditions for nucleation are favourable. Large contact angles on the other hand inhibit the process. Hienola et al. (2007) furthermore included line tension in the nucleation theorem via an additional factor in Young's equation.
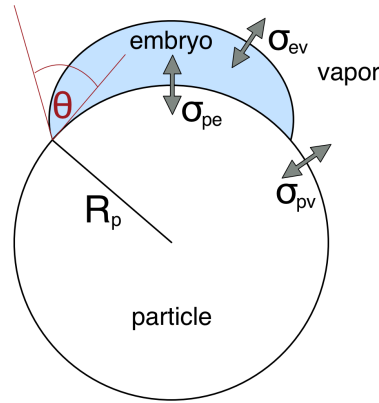
Figure 2.3: Embryo on pre-existing spherical particle, according to Fletcher (1958). With particle Radius R_p, contact angle θ and interfacial tensions, denoted as σ.

In addition to its geometrical features, other factors like chemical composition, surface charge (charging lowers the nucleation barrier (Winkler et al., 2008)), surface structure and wettability (Wang et al., 2018) also affect a particles capability to serve as a condensation nucleus. Hygroscopic, or soluble particles (with respect to the nucleating vapor) for example can trigger condensation even at saturation ratios below one. Since soluble particles just require such very low supersaturations of a few percent (i.e. a S_R of 1,01 equals 1% supersaturation S_s), they are the primary source for water droplet formation in the atmosphere, as every cloud droplet forms on a pre-existing particle. As seen in Figure 2.4 the critical supersaturation to activate particle growth decreases with increasing mass of soluble substances in the nucleus.

The combination of this solute effect, or Raoult's law and the Kelvin effect, which increases the vapor pressure in comparison to a flat surface is described by the **Köhler theory** (Seinfeld and Pandis, 2006). Each line in Figure 2.4 is one Köhler curve, which represents a specific $(NH_4)_2SO_2$ mass ratio. Köhler (1936) established the homonymous equation for water vapor and hygroscopic/soluble particles:

$$\ln\left(S_{R,d}\right) = \ln\left(\frac{p_{w,d}(D_p)}{p_{w,s}}\right) = \frac{4M_w\sigma_w}{RT\rho_w D_p} - \frac{6n_s M_w}{\pi\rho_w D_d^3}. \tag{2.14}$$

Where $S_{R,d}$ is the saturation ratio with respect to the droplet, defined via the water vapor pressure of the droplet $p_{w,d}$ and correspondingly of a flat surface $p_{w,s}$, M_w is the molecular mass of water, σ_w is the surface tension of the droplet, R is the gas constant, ρ_w the density of pure water and n_s is the number of moles of the solute. Based on Köhler theory, Petters and Kreidenweis (2007,2008,2013) developed the $\varkappa$-Köhler theory, where intrinsic particle properties are united in one parameter $\varkappa$.
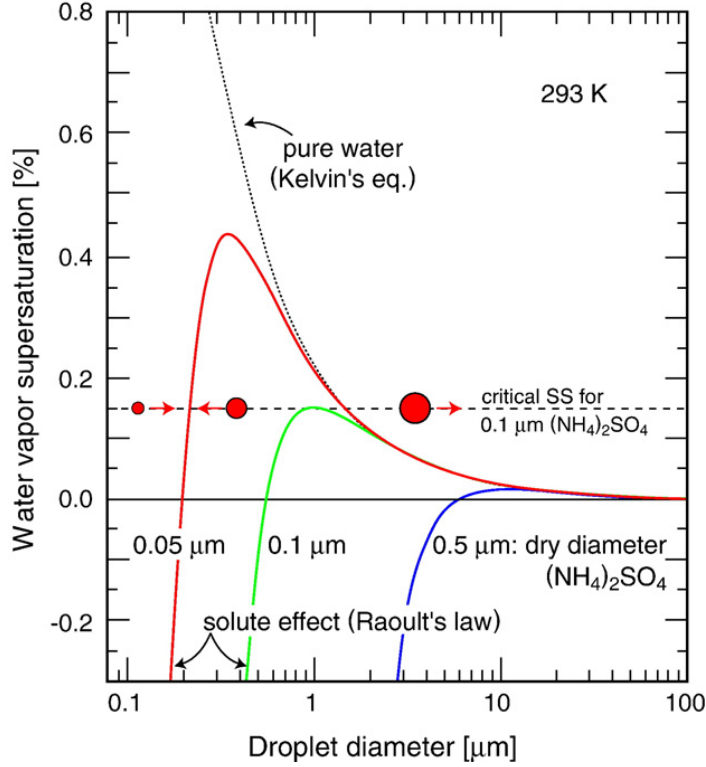
Figure 2.4: Köhler curves for droplets containing different initial masses of Ammonium Sulfite ($(NH_4)_2SO_2$) (Andreae and Rosenfeld, 2008; Seinfeld and Pandis, 2006).

2.2.4 Condensational Growth

Once a particle/droplet exceeds the critical diameter $D_d^* \equiv D_p^*$, independent of the formation process (whether homogeneous, or heterogeneous nucleation) condensational growth will take over. The growth-rate mainly depends on three parameters: the saturation ratio, particle diameter D_p and its relation to the mean free path λ of the vapor molecules (clusters). The latter can be divided into two regimes:

- **Random molecular collision ($D_p < \lambda$):**
  Via the kinetic theory of gases the rate of particle growth can be derived:

$$\frac{d(D_p)}{dt} = \frac{2M\alpha_c(p_\infty - p_d)}{\rho_p N_A \sqrt{2\pi M k_B T}}. \qquad (2.15)$$

Where M is the molecular mass, ρ_p is the density of the liquid, α_c is the condensation coefficient (i.e. the fraction of arrival molecules that stick to the droplets surface), p_∞ is the ambient and p_p the partial pressure at the surface of the droplet, N_A is the Avogadro's number, k_B the Boltzmann constant and T the temperature.

- **Diffusion of liquid molecules to the droplet's surface ($D_p > \lambda$):**
  This diffusion driven coagulation process can be illustrated as follows:

$$\frac{d(D_p)}{dt} = \frac{4MD_v}{R\rho_p D_p}\left(\frac{p_\infty}{T_\infty} - \frac{p_d}{T_d}\right)\Phi.\tag{2.16}$$

With the diffusion coefficient of the vapor D_v (the one of the droplet is negligible), the gas constant R, the temperature T_∞ away from and T_d at the droplets surface. Φ is the fuchs correction factor, which covers the region within one mean free path around the droplet, where the diffusion equation and the concept of a gradient break. The factor as derived by Davies (1978):

$$\Phi = \frac{2\lambda + D_p}{D_p + 533(\lambda^2/D_p) + 3,42\lambda}.\tag{2.17}$$

This effect slows down the growth rate of small particles, with decreasing particle size the importance of the factor grows (especially for particles of a size less than 0.1 μm).
For particles of sizes $D_p > \lambda$ the Kelvin effect can usually be neglected.

2.2.5 Heat and Mass Transfer

The key factor in assessing which seed particle sizes can be activated (heterogeneous nucleation) and grown into droplets in an environment where vapor is present is the saturation ratio S_R of that vapor. To obtain information about this parameter inside a CPC condenser tube, the heat and mass (of the vapor molecules) transfer processes can be considered. Mathematically, these processes can be described with partial differential equations (PDEs) (Zhang and Liu, 1990):

$$u\frac{\partial T}{\partial z} + v\frac{\partial T}{\partial r} = \frac{k}{\rho C}\left[\frac{\partial^2 T}{\partial z^2} + \frac{1}{r}\frac{\partial}{\partial r}\left(r\frac{\partial T}{\partial r}\right)\right],\tag{2.18}$$

$$u\frac{\partial n}{\partial z} + v\frac{\partial n}{\partial r} = D\left[\frac{\partial^2 n}{\partial z^2} + \frac{1}{r}\frac{\partial}{\partial r}\left(r\frac{\partial n}{\partial r}\right)\right].\tag{2.19}$$

With the temperature T in the heat transfer equation (2.18) and the vapor concentration n in the mass transfer equation (2.19). Where u is the axial component in z-direction and v the radial component in r-direction of the fluid velocity. D stands for the diffusion coefficient of the condensing vapor. k represents the thermal conductivity, C the specific heat and ρ the density of the carrier gas.

By solving both equations numerically, it is possible to determine S_R for each point in the condenser and thus the corresponding Kelvin diameter.

2.3 Particle Transport Loss Mechanisms

Aerosol particles inside a transport system can get lost due deposition onto the confining walls of that system. According to Hinds (1999), five basic mechanisms can be distinguished:

1. **Interception:**
   Appears when the streamline of a particle takes course too close to a surface, on which the particle is deposited.

2. **Inertial impaction:**
   Happens if a particle with high inertia can not follow a streamline, which is abruptly changing its direction.

3. **Diffusion:**
   Aersol particles get in contact with a surface, driven by random molecular collisions with gas molecules.

4. **Gravitational settling:**
   The gravitational force is always influencing aerosol particles, causing deposition.

5. **Electrostatic attraction:**
   If walls are not electrically conducting, an electric field is induced by charge separation, leading to particle losses.

Out of these five, diffusion is the one mechanism most important, regarding particles with diameters smaller than 100 nm (Hinds, 1999), which is the size range where CPCs are especially important.

2.3.1 Diffusion Losses

Diffusion is caused by Brownian motion of the aerosol particles and is defined as the net particle transport in a concentration gradient (from high to low) (Hinds, 1999). Walls of a transport system act as sinks, which creates an area of low concentrations (Weiden et al., 2009). The transport efficiency, i.e. the ratio of the number of aerosol particles leaving the transport system to the number entering it (Weiden et al., 2009), for a laminar flow in a circular tube, with respect to diffusion is given by (Kulkarni et al., 2011):

$$\eta_{diff}(D_p) = \exp\left(-\xi \cdot Sh\right). \tag{2.20}$$

Where $\xi = \pi D L / Q$, with the particle diffusion coefficient D, the lenght of the transport tube L and the volumetric flow rate Q. For the Sherwood number Sh, a formula by Holman (1972) can be used:

$$Sh = 3.66 + \frac{0.2672}{\xi + 0.10079 \cdot \xi^{1/3}}. \tag{2.21}$$

2.3.2 Other Effects

Besides the five main mechanisms for particle losses, other factors may also cause reduced transport efficiencies, of which some possibly are important for CPCs. A selection is listed below.

- **Stefan flow:**
  An aerodynamic flow, directed towards a condensing and away from an evaporating surface respectively.

- **Thermophoresis:**
  The movement of aerosol particles in a gas with a temperature gradient, towards the lower temperature.

- **Diffusiophoresis:**
  The displacement of particles in an environment consisting of two gas species, or rather a gas mixed with vapor, due to unequal momentum transfer between these two species.

2.4 Electrical Properties of Aerosol Particles

Electrical properties of aerosol particles are often utilized for experimental purposes, as in this study. In the following, a short overview of the concepts of electrical mobility and charging probability of aerosol particles is given.

2.4.1 Electrical Mobility

The electrical mobility Z, i.e. the ability of an aerosol particle to move according to an electrical field, can be utilized to select particles, depending on their diameter D_p. The quantity Z can be expressed as (Hinds, 1999):

$$Z = \frac{i e_0 C_C(D_p)}{3\pi\eta D_p}. \tag{2.22}$$

With the number n of elementary charges e_0 on the particle, the dynamical viscosity η of the gas and the Cunningham Correction factor C_c (Hinds, 1999).

$$C_C(D_p) = 1 + \frac{\lambda}{D_p} \cdot \left[2.34 + 0.15 \cdot \exp\left(-0.39 \cdot \frac{D_p}{\lambda} \right) \right], \tag{2.23}$$

where λ is the mean free path of the surrounding fluid (air). This factor is needed for small particle sizes approaching λ.

2.4.2 Charging Probability

The charging probability of aerosol particles is another important parameter, concerning the selection of particles, dependent on their diameter D_p. Many different theories concerning the process of charging spherical aerosol particles

have been developed, but the one provided by Fuchs (1963) appears to be most widely accepted (Reischl et al., 1996). Based on the theory, an estimation of the stable charging distribution and charging probability is possible, which is illustrated in Figure 2.5.
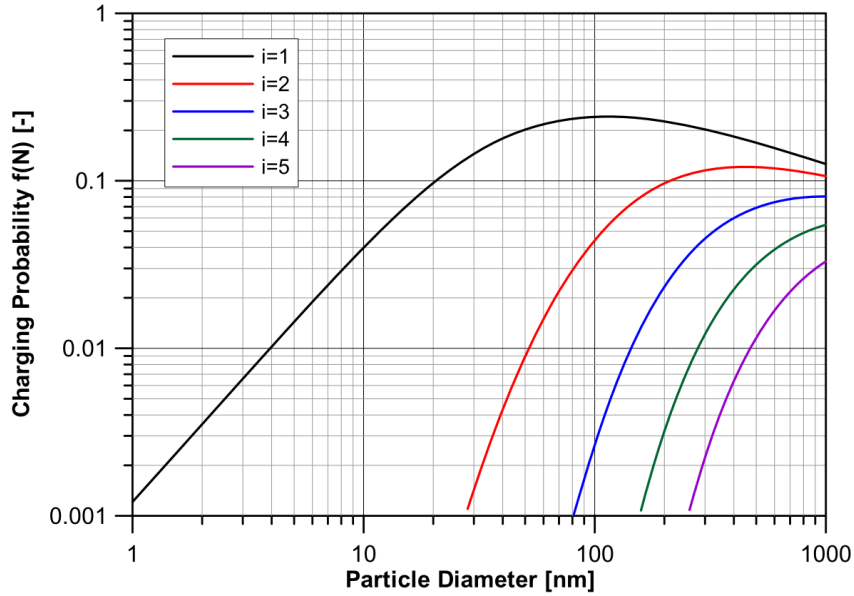
Figure 2.5: Fuchs charging probabilities for negatively charged aerosol particles, neutralized in a bipolar ionic atmosphere, with charging states i (see Equation 2.22) ranging from 1 to 5 (Steiner, 2011).

As visible in Figure 2.5, the probability for a particle carrying i elementary charges e_0 depends on the particle diameter D_p. For D_p smaller than roughly 20 nm, only singly charged ($i = 1$) or uncharged ($i = 0$) aerosol particles are present in a stable charge distribution. Larger particles are also able to carry multiple elementary charges ($i > 1$).

3 Methods

The experimental (subsection 3.1) and theoretical methods (subsection 3.2) applied in this study are presented below.

3.1 Experimental Methods

This section provides information on the experimental methods utilized in this study, to characterize CPCs at varying pressure conditions. The first part of the text is structured in the following way, always referring to aerosol particles:

Generation – Size Selection – Charging – Detection.

Succeeded by a description of the experimental setups and the data evaluation.

Whenever clean air is mentioned in the following (indicated by turquoise color in illustrations), it means that this air has been dried with silica gel and cleaned with HEPA (High-efficiency particulate air) and active carbon filters. Gas containing aerosol particles is indicated by red color arrows in illustrations.

3.1.1 Seed Particle Generation

Low pressure measurements with different aerosol particle species, as listed below, were conducted.

- **Silver particles** – Ag,

- **Sodium Chloride particles** (referred to as salt in the following) – NaCl,

- **Beta Caryolphyllene (BCy) particles** – $C_{15}H_{24}O_x$.

These particle types were chosen as representatives, for the various aerosol properties present in the Earth's atmosphere (see section 1). Silver and salt particles are widely used for CPC detection efficiency measurements (e.g. Hermann et al. (2007), TSI Incorporated (2016)). Additionally airborne sea-salt particles play an important role in the atmospheric system, being the largest aerosol component with respect to mass (Murphy et al., 2019; Liao et al., 2006). BCy incorporates the group of secondary organic aerosols (SOA), which arise from new particle formation processes in the atmosphere (Hallquist et al., 2009).

Depending on the particle material, different equipment and setups for aerosol generation were required. These are described in the following section.

17

3.1.1.1 Silver and NaCl Particles

A tube furnace was used to generate silver and NaCl seed particles. For this purpose, hydrophilic NaCl in its crystalline form (sodium chloride pro anaylsi), as well as hydrophobic silver wool for elemental analysis was utilized as source material (manufactured by Merck KGaA (64271 Darmstadt, Germany)). The tube furnace consists of a cylindrical housing with heatable walls, in which, along its radial center-line, a glass tube is placed. A glass crucible, carrying the desired seed particle material is inserted into that tube (see Figure 3.1).
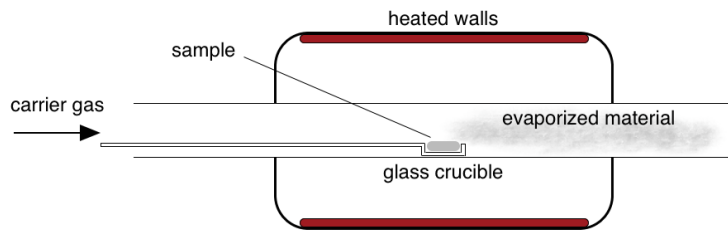
Figure 3.1: Schematic cross section of a tube furnace, with the crucible carrying a material sample.

The material placed on the crucible evaporates in the hot environment and is taken along with the carrier gas, which, in the case of this thesis is clean air. If a cooling path segment is connected right after the cylinder, homogeneous nucleation and condensation of the gaseous matter takes place within that part of the assembly, creating aerosol particles (Scheibel and Porstendörfer, 1983).

In this study, both silver and salt particles were generated by applying the aforementioned method of "evaporation and condensation". The difference in generation of these two particle types is the way cooling after the oven is accomplished, which depends on the operating temperature conditions inside the furnace and on the seed particle material.
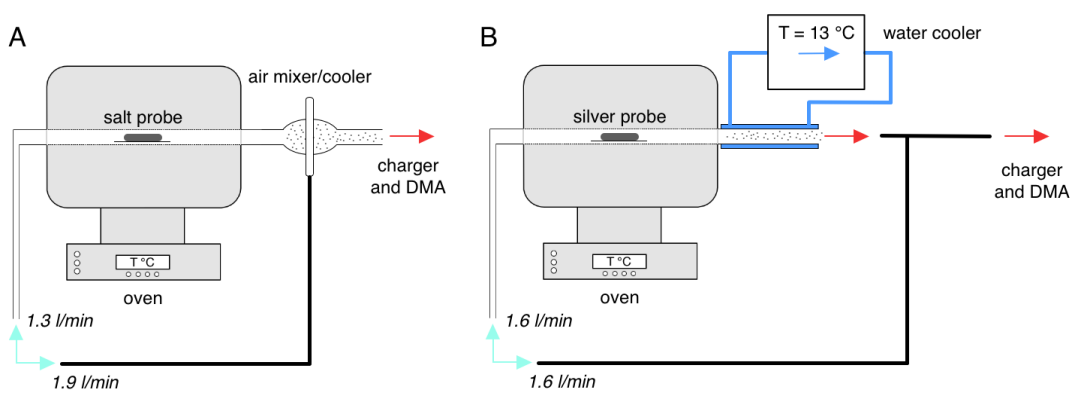
Figure 3.2: Schematic of the setups for salt particle generation (A) using a mixing alignment and silver particle generation (B) utilizing a water cooling system after the tube furnace.

As Scheibel and Porstendörfer (1983) describe, evaporation takes place above 600 °C working temperature of the oven for salt and above 900 °C for silver seed material. That is the reason, why subsequent mixing with clean air (at ambient temperature) is sufficient for NaCl particle generation and why water cooling is needed when silver is vaporized (see Figure 3.2). The hydrological cycle was regulated with a temperature control unit, which was set to 13 °C. Depending on the evaporation temperature inside the furnace, particle size distributions with varying concentration maxima can be produced, as can be seen in Figure 3.3 (for silver particles). In this study, temperatures were varied between 600 °C and 800 °C for salt and between 900 °C and 1100°C for silver particle generation.
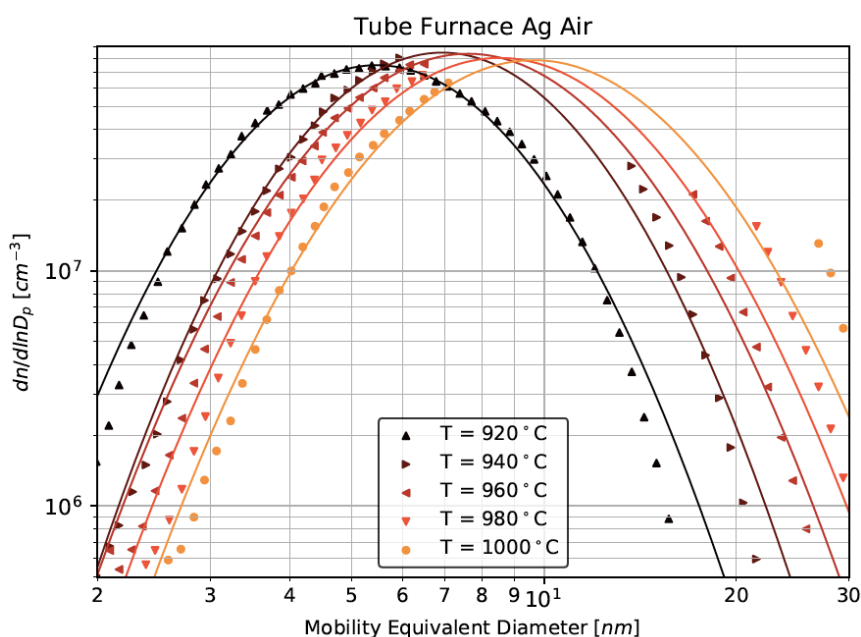
Figure 3.3: Silver particle size distributions for varying furnace temperatures with lognormal fits (Köberl, 2019).

3.1.1.2 BCy Particles

BCy particles were generated with a glass flow tube (Hearn et al., 2005), as it is described by Wlasits et al. (2020). Liquid $C_{15}H_{24}O_x$ (manufactured by Sigma-Aldrich (St. Lois, USA)) was vaporized with clean air and introduced into the tube, together with ozone (O_3), allowing ozonolysis reactions to take place and form SOA-particles, illustrated in Figure 3.4. The diameter of the tube equals 0.05 m and the length of the reaction path is adjustable from 0.1 to 0.4 m, with a movable piston. Variations of this parameter result in a shift of the mode diameter, of the corresponding particle size distribution. The temperature of the water basin, carrying the BCy was kept at 10°C and ozone concentrations, created with an UV lamp (custom made), were adjusted to 100-500 ppb (Wlasits et al., 2020).
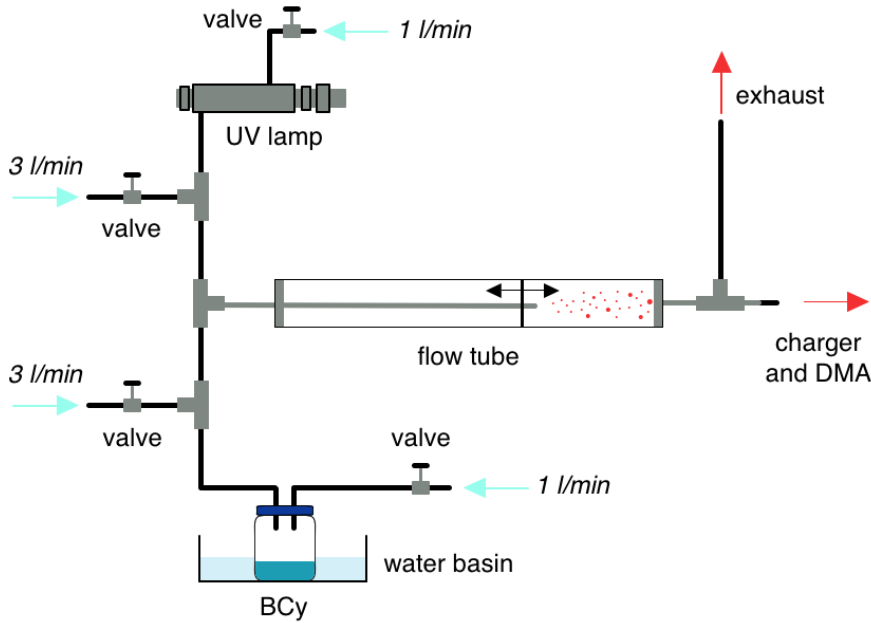
Figure 3.4: Schematic of the setup for BCy particle generation, consisting of BCy, a UV lamp and a flow tube.

3.1.2 Particle Size Selection

Particle size selection was accomplished with Vienna type differential mobility analyzers (DMAs), whose operation is based on electrical properties of said particles. The aerosol must therefore be brought into a stable state of charge (Reischl et al., 1996), before introduced into the DMA. To fulfill this requirement, the particles can be exposed to a sufficiently high number of positive and negative ions (Steiner, 2011), which was realized with a soft X-ray bipolar diffusion charger (TSI Advanced Aerosol Neutralizer 3088, see Figure 3.6). The Vienna type DMA itself consists of two cylindrical shaped electrodes fit into each other, to which voltage is applied (see Figure 3.5). The aerosol flow Q_a is introduced in the area between these electrodes and is therefore influenced by the present electrical field, which leads to a selection process, according to the individual electrical mobility Z of each particle. An extensive description of the Vienna type DMA is given by Steiner (2011) and the layout in this section is also mainly based on that work.

Equation 2.22 shows, that Z is dependent on the particle diameter D_p and DMAs take advantage of this fact. Particles carrying the opposing electrical charge, with respect to the polarity of the voltage applied to the inner electrode, drift towards the radial center of the cylinder. In this study, negatively charged particles were selected.
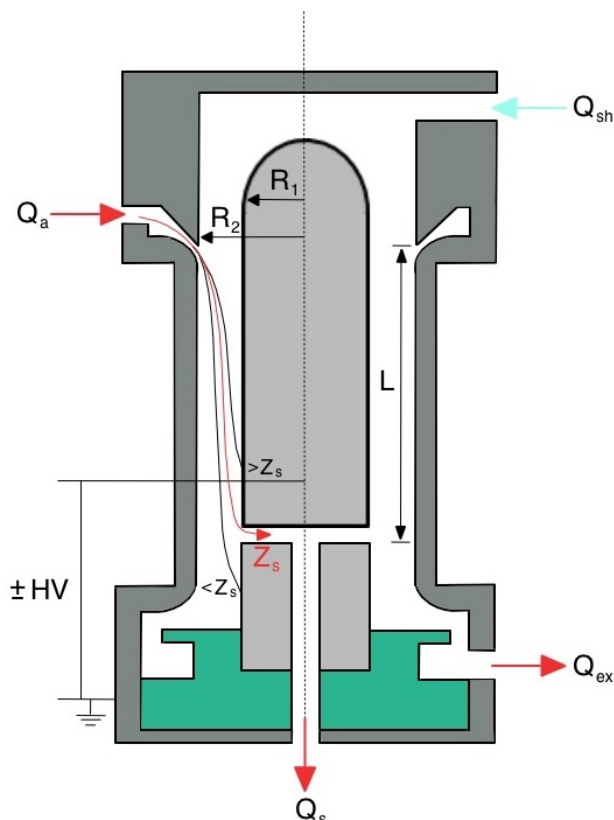
Figure 3.5: Schematic cross-section of a Vienna type DMA, in combination with a working principle illustration. Adapted from Steiner (2011).

A laminar sheath flow is achieved with a laminarization screen right after the Q_{sh} inlet. The tangential aerosol inlet, in combination with the curvature of the inner electrode in that region, provide a smooth transition of the aerosol into Q_{sh}. Shortly after that entering process, an equilibrium of forces, between the electrical - and the friction force (induced by Q_{sh}) is obtained. Depending on the voltage U, applied to the inner electrode, only particles with the correspondingly suitable electrical mobility Z_s reach the outlet (Q_s in Figure 3.5). All other particles, leave the DMA via Q_{ex}. This exit flow is dried, filtered and subsequently used for the sheath air flow again, as illustrated in Figure 3.6. In this manner, specific mobility bands can be filtered from a given aerosol particle size distribution.

The properties defining the operation of the DMA can be grouped as follows:

- **Geometry parameters** (as pictured in Figure 3.5 and 3.6):

    L – Effective axial distance between aerosol inlet and aerosol outlet,
    R_1 – Outer radius of the inner electrode,
    R_2 – Inner radius of the outer electrode.

- **Operating Conditions:**

Q_a – Aerosol flow rate,
Q_{sh} – Sheath air flow rate,
Q_{ex} – Excess air flow rate, $\Big\}$ approximately equal.
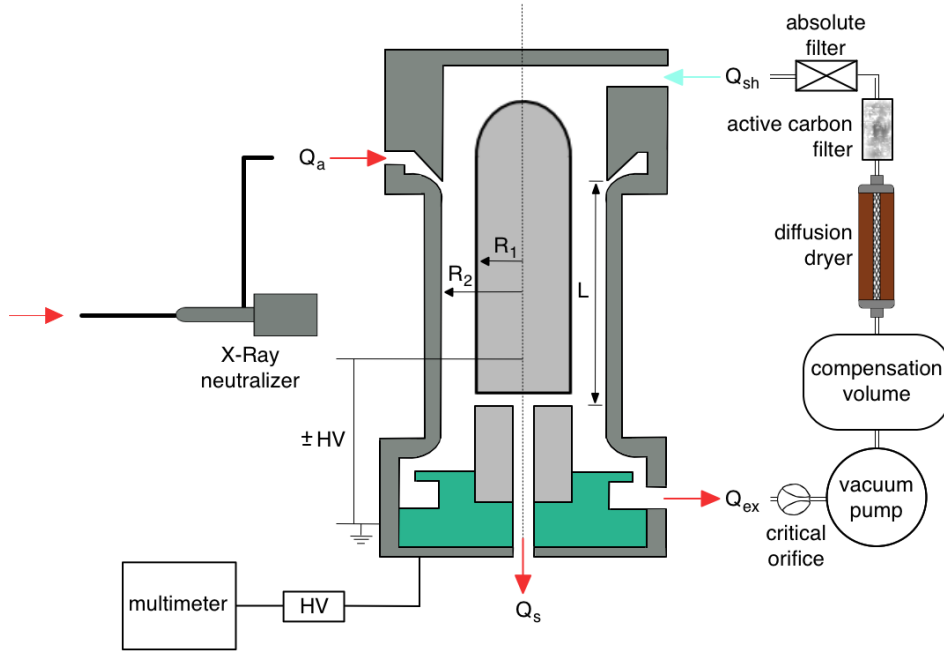
Figure 3.6: Vienna type DMA, together with the X-ray charger (see subsubsection 2.4.2) and the closed loop sheath air system. Illustration adapted from Steiner (2011).

If the operating conditions are kept constant, a unique relation between applied voltage and electrical mobility is the result:

$$Z = \frac{Q_{sh}}{U} \cdot \frac{\ln\left(R_2/R_1\right)}{2\pi L}. \tag{3.1}$$

Which implies, that a desired electrical mobility and in further consequence particle diameter can be selected, just by suitably adjusting the voltage U. The resolution R of a DMA (with respect to particle size) is given as:

$$R = \frac{Q_a + Q_s}{Q_{sh} + Q_{ex}}, \tag{3.2}$$

if flows are balanced and in the absence of diffusion (Flagan, 1999).

3.1.2.1 DMA Operation and Multiple Charge Considerations

The DMA used for the measurements had the following dimensions (see DMA 3/150 in Winklmayr et al. (1991)):

- $L = 150$ mm,

- $R_1 = 25$ mm,

- $R_2 = 33$ mm.

The sheath flow rate was kept constant with a critical orifice, at $Q_{sh} = 25$ l/min.

As mentioned before, DMAs select particles dependent on their electrical mobility Z, which amongst other factors is proportional to the number of elementary charges e_0 carried by the particle. Via the soft X-ray charger, a defined charging state (referring to Figure 2.5) was achieved, in all setups. In this way, no additional considerations, besides the corresponding voltage applied to the DMA were necessary for particle diameters of up to about 20 nm. Due to the fact, that only singly charged (and uncharged) particles are present, at such small Z, in a stable charge distribution.

For $D_p > 20$ nm, where larger, multiply charged particles with the same Z are more likely to be found, the approach described in the following, appeared to provide adequate results.
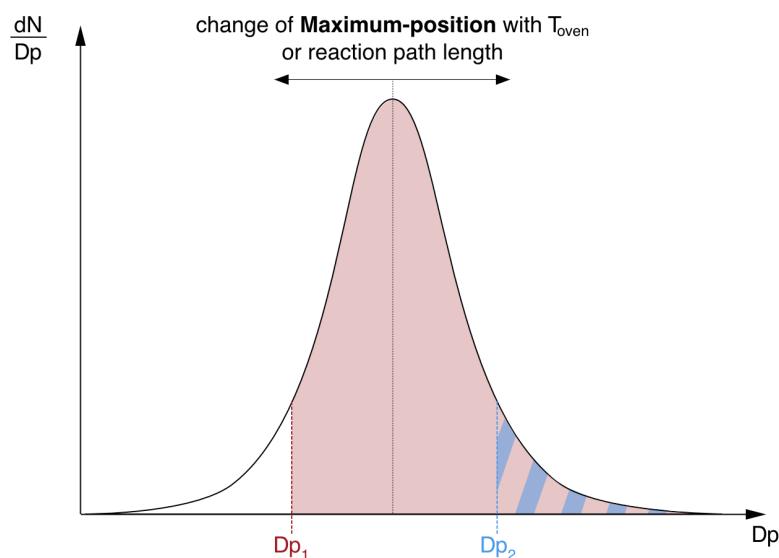
Figure 3.7: Exemplary particle size distribution, as generated by the methods described in subsubsection 3.1.1 (black line). Red and blue highlighted areas mark the number concentration ranges available for possible multiple charged particles, according to $D_{p,1}$ and $D_{p,2}$.

Depending on the temperature inside the furnace, or the length of the reaction path (flow tube), the particle generation mechanisms mentioned in subsubsection 3.1.1 produce size distributions with varying concentration maxima, as indicated in Figure 3.7. By adjusting the generation conditions, in a way that the desired particle size D_p (with $i = 1$) lies to the right hand side of the size distribution maximum (see $D_{p,2}$ in Figure 3.7), no significant particle concentration is available at the particle diameter for which double charge would result in the same Z. If the voltage settings at the DMA cause a selection of a particle size with $i = 1$ on the left hand side of the distribution maximum (see $D_{p,1}$ in Figure 3.7), chances are very high that many double charged particles are present at the corresponding Z. Such circumstances lead to an overestimation of the number concentration by the FCE, if it is set to $i = 1$, since every particle carrying two elementary charges is counted doubly (particle size independent measurement).

Equations 2.22 and 3.1 can be combined and the result converted for the voltage U applied to the inner electrode:

$$U = \frac{3\pi\eta D_p}{i e_0 C_C(D_p)} \cdot \frac{Q \cdot \ln(R_2/R_1)}{2\pi L}. \tag{3.3}$$

By plugging in all known values, the voltages necessary to select the desired particle sizes can be derived. With the elementary charge $e_0 = 1.6 \cdot 10^{-19}$ C and the dynamic viscosity of air $\eta = 1.84 \cdot 10^{-5}$ Pa·s at standard conditions. The results are listed in Table 3.1.

Table 3.1: Particle diameters D_p with corresponding voltages U and diameters of double charged $D_{p,double}$ particles with the same Z.

D_p [nm]	$D_{p,double}$ [nm]	U [V]
7	–	29
10	–	59
20	–	231
30	43	504
50	73	1319
100	151	4571

In the central column of Table 3.1, the diameters of double charged particles ($i = 2$) are listed. The values correspond to the particles carrying one elementary charge ($i = 1$) in the first column, which have the same electrical mobility Z. The diameters $D_{p,double}$ were obtained by using this equality and Equation 2.22:

$$\frac{i_1 e_0 C_C(D_{p,1})}{3\pi\eta D_{p,1}} = \frac{i_2 e_0 C_C(D_{p,2})}{3\pi\eta D_{p,2}},$$
$$i_1 \frac{D_{p,2}}{C_C(D_{p,2})} = i_2 \frac{D_{p,1}}{C_C(D_{p,1})}. \tag{3.4}$$

With $i_1 = 1$, $i_2 = 2$ and a numerical approach to find $D_{p,2} = D_{p,double}$, fulfilling relation 3.4.

In practice, the voltage for the desired particle diameter was set and the furnace temperature, or the reaction path length (depending on the particle generation process) were adjusted in a way, that particle concentrations of about $3 \cdot 10^4$ cm^{-3} were detected by the instruments. Possible multiple charges were subsequently verified by applying the voltage to the DMA, needed to select the corresponding $D_{p,double}$ (for $i = 1$). If the concentration measured at these conditions were lower than 100 cm^{-3}, it was considered that the size distribution delivered by the particle generator was suitable for the measurement.

3.1.3 Particle Detection

In the course of this study, particles were detected using two different experimental concepts. On one hand CPCs were used, as the general instruments of interest, on the other hand a Faraday cup electrometer (FCE) provided the needed reference for particle number concentration. Both instrument types, as well as their physical working principles are described in the following sections.

3.1.3.1 Conductive Cooling CPC

As a conductive cooling type CPC, the TSI 3772-CEN works with a continuous flow. Its principle of operation is based on diffusion cooling to induce supersaturation of a working fluid vapor and subsequently condensational growth of introduced aerosol particles. This type of CPCs consists of saturator, condenser and optics block. General aspects about these instruments and their working principle are described in the following (mainly based on Kulkarni et al. (2011)), before details of the TSI 3772-CEN CPC are outlined.

Particle Activation and Growth

Conductive cooling CPCs utilize alcohol (such as n-butanol or isopropanol) as a working fluid, which is kept at an elevated temperature in the saturator. The aerosol stream is introduced and the residence time is such that the aerosol becomes saturated with the alcohol vapor at the present temperature. Subsequently the stream enters the condenser tube, in which a lower temperature is set and controlled by cooled walls. Conductive cooling from the walls to the stream takes place. Since this heat transfer is faster than the mass transfer of the alcohol vapor molecules to the walls, supersaturation occurs. The temporal difference in transfer rates is caused by the high mass and inertia of the alcohol molecules. Due to the strong temperature dependence of $p_S(T)$, it decreases faster than p_v, resulting in supersaturated conditions (see Equation 2.3).
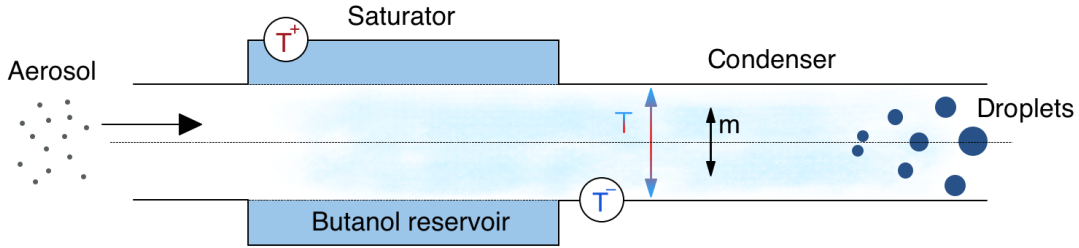
Figure 3.8: Schematic of the particle growth mechanism inside a conductive cooling CPC. T^+ denotes the higher temperature of the saturator walls, whereas T^- respectively marks the lower temperature in the condenser. The arrows within the condenser refer to mass- and accordingly temperature transfer to the walls.

The smallest particle size that will grow in the condenser, correspondent to the achieved supersaturation S_S is equal to the Kelvin diameter D_d^* from Equation 2.7. All activated nuclei grow to a size of about 10 μm in diameter, regardless of their initial size (Hinds, 1999). Altering the temperature settings (i.e. increasing ΔT between saturator and condenser) can lower the cut-off diameter of a CPC. If this temperature difference becomes too big (depending on CPC model) homogeneous nucleation occurs and the measured number concentration will exceed the primary aerosol particle concentration (Kangasluoma et al., 2015).

Detection Efficiency and Cutoff Diameter

According to Stolzenburg and McMurry (1991), the total detection efficiency η_{tot} of a CPC can be written as follows:

$$\eta_{tot}(D_p) = \eta_s(D_p) \cdot \eta_a(D_p) \cdot \eta_c(D_p). \tag{3.5}$$

Where η_s is the sampling efficiency, accounting for internal particle losses, given by the ratio of particles exiting and entering the instrument. The factor η_a, called activation probability, takes the nucleation and condensation processes into account and is influenced by the saturation ratio reached in the condenser. Finally, the counting efficiency η_c considers the performance of the optical detection system.

As already mentioned in section 1, the cutoff diameter D_{50} marks the particle size, at which the detection efficiency of a CPC reaches 50 %, with respect to a reference instrument (see paragraph 3.1.3.2).

Coincidence

As explained in Hinds (1999), coincidence is a form of an error arising for optical measurement methods, at high particle number concentrations N.
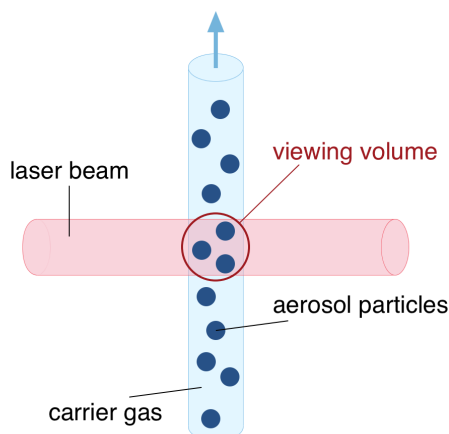
Figure 3.9: Illustration of coincidence in optical particle measurement systems. Multiple particles are simultaneously present in the viewing volume (i.e. the part of the aerosol stream illuminated by the laser beam).

Coincidence occurs, if more than one particle at a time is present in the viewing volume covered by the laser beam, as depicted in Figure 3.9, resulting in an underestimation of N. It causes an upper concentration limit N_{max}, reliably detectable with a given optical system. The ratio of the measured number concentration N_0 to the actual one N_i is given by (Hinds, 1999):

$$\frac{N_0}{N_i} = \exp\left(-N_i Q \tau\right) \tag{3.6}$$

Where Q is the aerosol flow rate and τ is the time it takes a particle to traverse the viewing volume.

TSI 3772-CEN

The TSI 3772-CEN CPC weighs 5.5 kg and is sensitive to tilting, as n-butanol CPCs generally are, which needs to be considered regarding airborne campaigns. The internal setup of the instrument is shown in Figure 3.10, it can be divided into three categories (TSI Incorporated, 2007, 2016):

- **The Sensor:**
  The sensor consists of saturator, condenser and an optical detector. The saturator is a cylindrical, n-butanol soaked wick, through which the aerosol stream passes and gets saturated. The cylinder is kept at an elevated temperature of 39°C. The n-butanol is replenished from a reservoir and a removable fill bottle. In the condenser tube, the stream is subsequently cooled by a thermoelectric device set to 18°C, so that nucleation and condensational growth occurs. As a result, the CPC features a cutoff diameter D_{50} of 7 nm for silver particles, whereas the maximum detectable particle diameter is above 3 μm. Condensed liquid on the walls of the condenser tube flows back to the wick for reuse. Afterwards the aerosol enters

the optical detector through a nozzle. The detection system consists of a laser diode, a photodiode detector as a counterpart and a system of lenses between these two components. After exiting the laser diode, the light passes a collimating and a focusing lens, so that the beam is focused, when it transverses the aerosol stream. Subsequently a pair of aspheric collection lenses guide the scattered light onto a low noise photodiode. A reference photodiode is used to maintain constant laser power output. The housing containing the optics is kept at an elevated temperature of 40 °C, higher than the saturator temperature, to avoid condensation of the working fluid on the lens surfaces. The upper limit of detectable particle number concentration with this sensor system is specified as $5 \cdot 10^4$ cm^{-3}, beyond that limit, coincidence can not be corrected for.
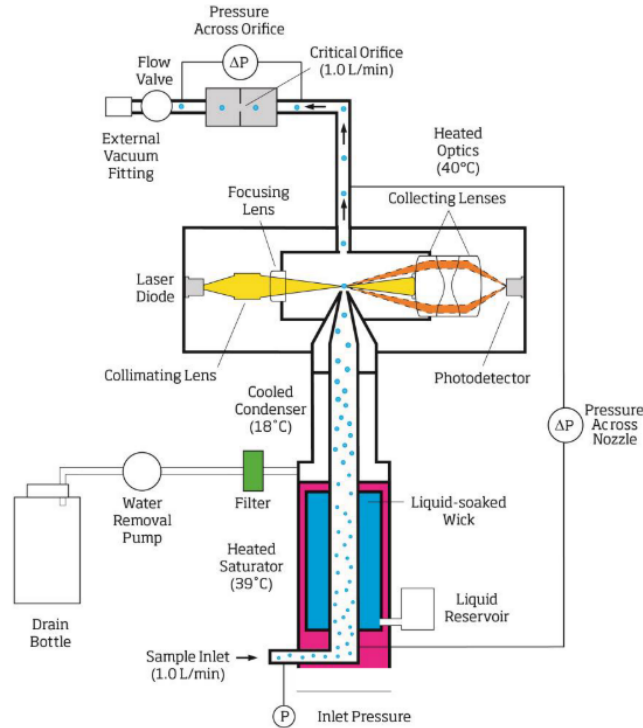
Figure 3.10: Schematic of the TSI 3772-CEN condensation particle counter (TSI Incorporated, 2015).

- **The Flow System:**
  A constant critical flow of 1 l/min is achieved via an orifice and an external pump, generating a critical pressure ratio. Critical flow is stable, providing a constant volumetric flow, despite varied inlet pressures. The pressure ratio can be found by dividing the absolute pressure downstream p_d, by the absolute pressure upstream p_u of the orifice. For air, the following relation must hold for critical pressure p_{crit} and thus critical flow (Potter et al., 2010):

$$p_{crit} = \frac{p_d}{p_u} \leq 0.528. \tag{3.7}$$

- **Signal Processing Electronics:**
  Microprocessor signal processing electronics convert the optical signals received from the photodiode into digital data, enabling further analysis.

3.1.3.2 Reference Instrument – Faraday Cup Electrometer

As described in Kulkarni et al. (2011), a Faraday cup electrometer (FCE) is the simplest particle detector, based on sensitive current amplifying. A schematic of the used TSI 3068B FCE (TSI Incorporated, 2006) is depicted in Figure 3.11. Basically, charged aerosol particles are captured by a high efficiency conductive filter, connected to an electrometer current sensor (ground). The filter is embedded in a metal housing, from which it is isolated, constituting as a "Faraday cup". Particles hitting the filter get neutralized by electron exchange with the ground, resulting in a detectable electrical current, proportional to the collection rate on the filter. As displayed in Figure 3.11, an additional outer metal housing, isolated from the inner setup, surrounds the Faraday cup to shield it from stray electric fields.
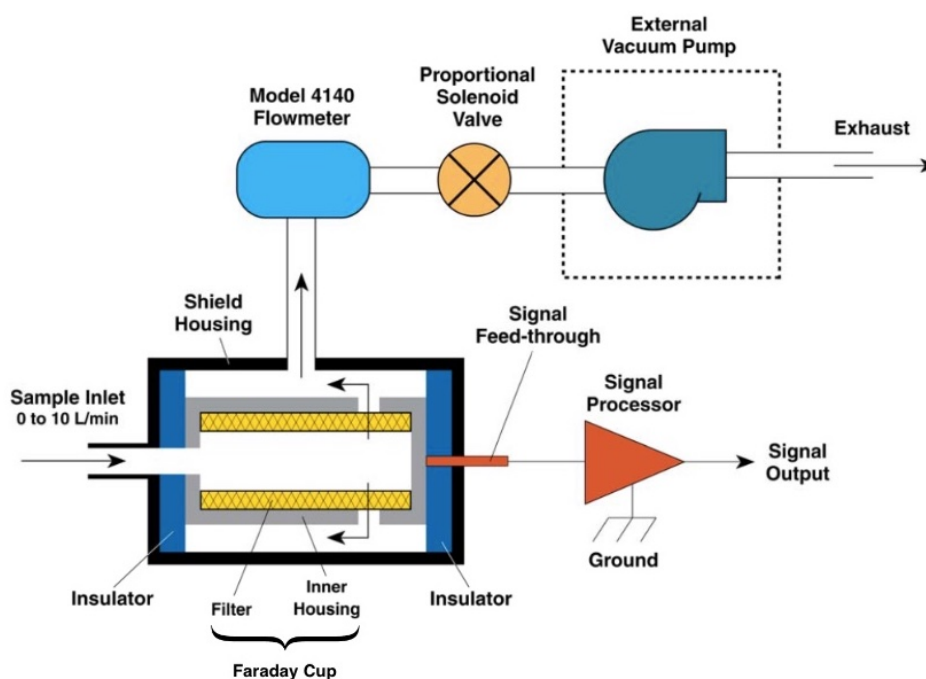
Figure 3.11: Schematic of the TSI 3068B Faraday Cup Electrometer (TSI Incorporated, 2006).

At favourable conditions, so defined charge state of the particles and known aerosol flow rate, the following relation can be utilized to calculate the particle number concentration (TSI Incorporated, 2006):

$$I = N \cdot i \cdot e_0 \cdot Q_a. \tag{3.8}$$

Where I denotes the electrical current, detected by the instruments sensor. As before in subsubsection 3.1.2, i marks the number of elementary charges e_0, carried by one particle and Q_a labels the aerosol flow rate. This rate can be adjusted with a combination of an internal proportional solenoid valve and a mass flow meter, allowing flows between 0.3 and 10 l/min. In this study it was set to 1 l/min, to match the CPCs.

According to Pihlava et al. (2016), two components make up the current measured by an FCE. First, the actual signal induced by the charged particles and secondly an offset signal, caused by disturbances, such as electric current noise. The offset is dependent on environmental factors (e.g. temperature or humidity) and thus can vary with time. At low particle concentrations, noise covering the desired signal, causes high uncertainties, limiting the range of reliable measurements for FCEs (Yang et al., 2018).

3.1.4 Experimental Setups and Measurement Method

The setups to characterize the TSI 3772-CEN CPC detection efficiency at various pressure rates are described in the following. To avoid flooding of the CPCs, the n-butanol fill bottles were disconnected and the feature 'autofill' was deactivated during every measurement cycle (where one cycle consists of one measurement at every pressure step). After the completion of one cycle (which took a maximum time of about three hours), the system was brought back to ambient pressure and the fill bottles were reconnected, to supply the saturators with n-butanol.

3.1.4.1 Detection Efficiency Measurements for Silver and Sodium Chloride Particles

A schematic of the setup used for the pressure dependent detection efficiency measurements of silver and salt particles is illustrated in Figure 3.12. The volumetric flow rates adjusted for particle generation are enlisted in Table 3.2. $Q_{furnace}$ labels the flow rate through the furnace and $Q_{dilution}$ denotes the clean air flow rate used for dilution or rather cooling, in the case of salt.

Table 3.2: Flow rate settings for silver and salt particle generation.

	$Q_{furnace}$ [l/min]	$Q_{dilution}$ [l/min]
Ag	1.6 ± 0.1	1.6 ± 0.1
NaCl	1.3 ± 0.1	1.9 ± 0.1

Subsequent to the generation process, particles were transported (via conductive tubing) to the X-ray charger and the DMA for size selection. A T-piece then divided the flow into two parts, one of which was routed to the instrumentation

and one directly connected to the exhaust, taking the excessive flow coming from the DMA into account. The part of the aerosol flow directed to the particle detection segment was then passed through a needle valve, used to reduce the pressure within the downstream setup-part, by adequately decreasing the valve's diameter. To monitor the resulting lower pressure, with respect to the ambient level, a pressure sensor (model DELOS SI) produced by JUMO Mess- und Regelgeräte GmbH (Vienna, Austria) was used.
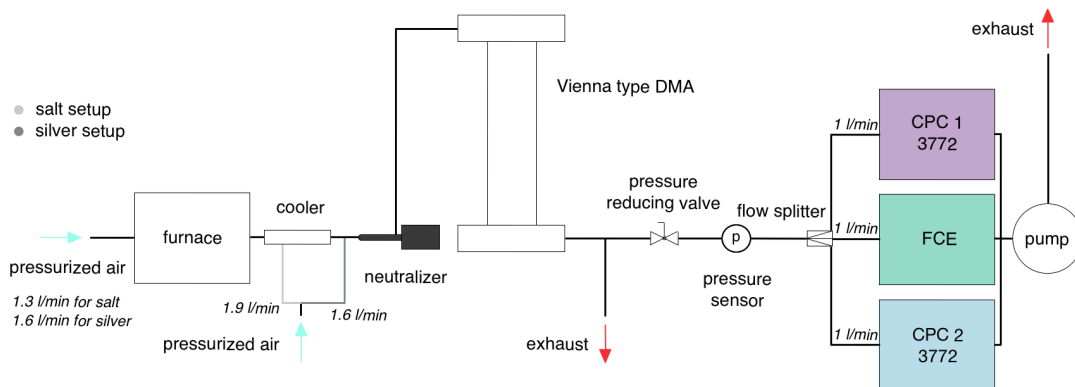
Figure 3.12: Schematic of the setup for the detection efficiency measurements at various pressure rates for silver and salt particles.

Measurements were performed at pressure steps of 100 hPa from 1000 to 500 hPa and in 50 hPa steps from 500 to 150 hPa. Following the pressure reduction, a flow splitter was utilized to divide the aerosol stream to the three counting instruments. Each with a flow rate of 1 l/min, whereas the FCE was adjusted to match the CPCs. All three instruments were attached to the same Agilent IDP-3 dry scroll pump (Santa Clara, USA), which was responsible for the low pressure generation in collaboration with the valve.

3.1.4.2   Detection Efficiency Measurements for BCy

The setup used for the pressure dependent detection efficiency measurements of BCy particles is illustrated schematically in Figure 3.13. The flow rates concerning the particle generation process are listed in Table 3.3, where Q_{agent} denotes the flow through the ozone lamp or the BCy solution reservoir respectively.

Table 3.3: Flow rate settings for BCy particle generation.

	Q_{agent} [l/min]	$Q_{dilution}$ [l/min]
$C_{15}H_{24}O_x$	1.0 ± 0.1	3.0 ± 0.1
O_3	1.0 ± 0.1	3.0 ± 0.1

Resulting particle concentrations were varied by adjustments on the UV lamp (adjustments of reaction space). To avoid high total flow trough the DMA,

which would cause a decrease in its resolution R, an exhaust was placed between the flow tube and the charger. In this configuration, the pump pulled the aerosol sample through the DMA at a desired lower flow rate of 3 l/min.
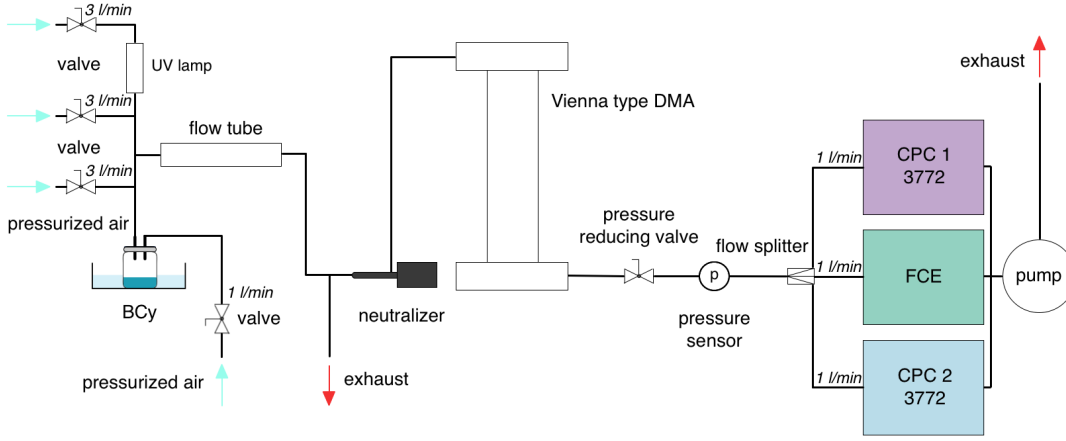
Figure 3.13: Schematic of the setup for the detection efficiency measurements at various pressure rates for BCy particles.

The remaining parts of the setup after the DMA, so pressure reduction and particle detection, follow the description given in the previous section.

3.1.5 Data Evaluation

3.1.5.1 Particle Number Concentration

Generally, particle number concentrations were always kept between 2000 and $3 \cdot 10^4$ particles per cm^3, to be safely above the FCE background noise level on the lower end and avoid coincidence inside the CPC on the upper limit. Every data point presented in section 4 is the result of a one minute measurement average.

Particle number concentrations measured with the FCE are calculated in the instruments software, according to Equation 3.8, with i set to 1 and an aerosol flow rate of $Q_a = 1$ l/min. The latter was verified with a TSI 4140 mass flow meter (MFM).

The 3772 CPCs do also have the ability to directly calculate number concentrations from detected counts. To do so, the flow of 1 l/min created by the critical orifice is utilized. However, in this study, the raw counts recorded by the instruments were used to obtain the particle number concentrations. Equation 3.6 was utilized and rearranged:

$$N_i = N_0 \exp\left(N_i Q \tau\right). \tag{3.9}$$

Where the N_i located in the exponent, was estimated with N_0, which was calculated as follows:

$$N_0 = \frac{n_{counts}/s}{Q_a}.$$ (3.10)

Here n_{counts} denotes the raw count number, detected by the CPC. The factor τ in the exponent of Equation 3.9 was taken as 0.35 µs from the manual (TSI Incorporated, 2007). In this way, particle number concentrations were calculated, based on the actual flow rates at every pressure step (mesured with the TSI 4140 MFM, see subsubsection 4.1.1), in combination with coincidence correction.

3.1.5.2   Detection Efficiency

Detection efficiencies were calculated as the ratios between number concentrations measured by the CPC and the FCE, as a function of particle diameter D_p and pressure p:

$$\eta(D_p, p) = \frac{N_{CPC}(D_p, p)}{N_{FCE}(D_p, p)}.$$ (3.11)

As discussed before, D_p was controlled with the voltage, applied to the DMA and p with the valve placed before the particle detection section of the setup.

Plots for each particle type were created, with the pressure rates on the x- and detection efficiencies on the y-axis. Together, data-points for fixed particle diameters lead to "cutoff" curves, depending on pressure. An empirical function was developed to fit these curves:

$$f(\eta) = a \cdot e^{-\exp\left[-k\cdot(\eta-\eta_0)\right]} \cdot (b - e^{-n\cdot\eta}) \cdot \eta^c.$$ (3.12)

The factors occurring in Equation 3.12 and their geometric meaning are listed in Table 3.4.

Table 3.4: Parameters used in the empirical fit function $f(\eta)$ for the detection efficiency curves.

parameter	association
a, b	position of the plateau (η)
k	curvature
η_0	offset (on x-axis)
n	n-th root function
c	curvature of the plateau

3.1.5.3 Uncertainties

Systematic uncertainties, caused by the instruments were used for data analysis, since it was found that they predominate the statistical uncertainties. Table 3.5 sums up the corresponding values for the utilized instruments.

Table 3.5: Systematic uncertainties of the used instruments (TSI Incorporated, 2016, 2006). For the MFM and the pressure sensor, respectively the last stable digit displayed was taken as uncertainty.

instrument	quantity	uncertainty
TSI 3772-CEN CPC	N	10.0 %
TSI 3068B FCE	N	5.0 %
TSI mass flowmeter	Q	0.1 l/min
JUMO pressure sensor	p	10 hPa

The quantities presented in Table 3.5 in combination with Gaussian error propagation were taken into account to obtain the uncertainties for each data point separately.

Additionally to these uncertainties, the selected particle diameter is also afflicted with an uncertainty, given by the DMA resolution R (see Equation 3.2). With $Q_{sh} = Q_{ex} = 25$ l/min and $Q_a = Q_s = 3$ l/min for BCy particles and 3.2 l/min for silver and salt particles respectively, R took values between 0.12 and 0.128 in the measurements.

3.2 Theoretical Methods

Theoretical evaluations of the measured detection efficiencies of the TSI 3772-CEN CPC were performed, via simulations of the supersaturation profiles inside the condenser of the instrument. The proceeding in this study basically follows the approach presented by Tauber, Steiner and Winkler (2019). With FEniCS (Langtangen and Logg, 2016), a finite element model was developed. Convective, as well as diffusive heat and mass transfer processes were simulated, to obtain saturation ratios at every position within the condenser tube.
In addition, possible losses due to diffusion inside the CPCs were considered, by utilizing the particle loss calculator (Weiden et al., 2009).

3.2.1 Simulation of Heat and Mass Transfer

The transfer equations for both considered processes were solved by assuming a fully developed laminar flow, using the following hyperbolic profile for a straight circular pipe (Kutin and Bajsic, 2014):

$$v(r) = 2v_{avg} \cdot \left(1 - \frac{r^2}{R^2}\right). \qquad (3.13)$$

Where R is the inner radius of the condenser tube and v_{avg} is the average velocity, which can be calculated from the aerosol flow rate Q_{aero} as:

$$v_{avg} = \frac{Q_{aero}}{A} = \frac{Q_{aero}}{\pi R^2}. \tag{3.14}$$

The partial differential equations 2.18 and 2.19 can be transformed as follows (with a radial velocity component v of 0 and inserting the laminar flow profile for the axial velocity component u):

$$c \cdot v(r) \cdot \frac{\partial \Psi}{\partial z} = P_e \cdot (1 - r^2) \cdot \frac{\partial \Psi}{\partial z} = \frac{\partial^2 \Psi}{\partial r^2} + \frac{1}{r} \cdot \frac{\partial \Psi}{\partial r} + \frac{\partial^2 \Psi}{\partial z^2}. \tag{3.15}$$

Where the inner radius R of the condenser tube is set to one for the simulations. The variable Ψ can be replaced with the temperature T to calculate the heat transfer and in the case of mass transfer with the vapor pressure p_v. The factor c represents the inverse of the coefficients on the right hand side of equations 2.18 and 2.19, for heat or mass transfer accordingly. The Peclet number P_e must be adjusted respectively as well (Zhang and Liu, 1990):

$$P_{e,T} = Re \cdot Pr, \tag{3.16}$$

$$P_{e,P_v} = Re \cdot Sc. \tag{3.17}$$

Here Re, Pr and Sc are Reynolds, Prantl and Schmidt number respectively:

$$Re = \frac{\rho \cdot v_{avg} \cdot 2R}{\mu}, \tag{3.18}$$

$$Pr = \frac{\nu}{\alpha} = \frac{\mu/\rho}{k/(\rho \cdot C)} = \frac{\mu \cdot C}{k}, \tag{3.19}$$

$$Sc = \frac{\nu}{D} = \frac{\mu}{\rho \cdot D}. \tag{3.20}$$

These three dimensionless parameters, characterize the fluid flow (Re), as well as physical properties of carrier gas and working fluid vapor (Pr and Sc). In the equations 3.18-3.20, ρ represents the density of the carrier gas (air), μ is the dynamic - and ν the kinematic viscosity. Furthermore, α is the thermal diffusivity of air, k the thermal conductivity and C the specific heat capacity. Finally D stands for the diffusion coefficient of the condensing vapor (n-butanol).

As can be seen from Equation 3.15, the only pressure dependent component in the transfer processes is the respective Peclet number. In particular, the Reynolds number, which is inverse proportional to the pressure. According to Zhang and Liu (1990), the Schmidt number is independent and the Prantl number virtually independent of pressure. Consequently, Re was assumed to be the only pressure relevant element for calculations of the Peclet numbers at various pressure conditions.

3.2.1.1 Simulation Parameters

Following the remarks in Kangasluoma et al. (2015), the length of the condenser tubes was assumed to be 85 mm and the inner diameter 5 mm. Since the aerosol stream is split into 8 paths through saturator and condenser, the volumetric flow rate in each of these tubes is 1/8 l/min. Additionally, the aerosol flow was assumed to be uniformly saturated at the inlet of the condenser.

Values of partial vapor pressure were calculated using the Antoine equation (DDBST, Dortmund Data Bank (DDB), n.d.). Utilizing equations 3.16 to 3.20, the Peclet numbers for ambient pressure rates, ranging from 30 hPa to 1000 hPa were calculated. The results of these computations were validated by comparing them with values presented by Stolzenburg and McMurry (1991).

Table 3.6: Boundary conditions for temperature T and mass transfer (partial vapor pressure p_v).

	T [°C]	p_v [mbar]
Condenser inlet	39.0	23.7
Condenser walls	18.0	5.5

3.2.1.2 Activation Efficiency

Theoretical activation efficiencies η_{act} were derived, utilizing the two parameter formula established by Stolzenburg and McMurry (1991):

$$\eta_{act}(D_p) = 1 - \exp\left(-log(2) \cdot \frac{D_p - D_0}{D_{50} - D_0}\right). \tag{3.21}$$

Here D_0 and D_{50} represent the particle diameters for 0 % and 50 % activation efficiency respectively. Both quantities were calculated using the Kelvin equation with n-butanol properties taken from Lapuerta et al. (2014). The corresponding saturation ratios and temperatures were extracted from the simulated profiles (see Figure 4.11). For D_0 the maximum supersaturation occurring at the centerline (r=0) was used. The aerosol particle concentration is assumed to be virtually evenly distributed across the whole flow cross section. Following this approach, D_{50} was estimated by taking the peak S_R at r/2, since 50 % of all particles experience at least that level of supersaturation.

3.2.2 Diffusion Losses

To achieve a better representation of the actual experimental situation, diffusion losses of aerosol particles were also taken into account, utilizing the particle loss calculator (PLC; Weiden et al., 2009). This software tool uses the formulas presented in subsection 2.3 to compute the transport efficiencies (with respect

to diffusion) for varying ambient conditions, depending on particle diameter. To reproduce experimental conditions, tubing inside the CPC was considered. Losses inside the FCE were not included, since the Faraday cup is located right after the aerosol inlet of the instrument, resulting in a negligible tube length. The parameters displayed in Table 3.7 were constant for all calculations.

Table 3.7: Fixed parameters for particle diffusion transport loss evaluations.

$T_{ambient}$ [°C]	$\rho_{particle}$ [g/cm^3]	shape factor
25	1.5	1

The particles were assumed to be perfect spheres, hence the shape factor (a correction parameter to account for changes in particle motion, due to the particle's shape (Hinds, 1999)) of one . An approximated value of the particle density for silver was used (see Liao et al. (2018)).

The aerosol inlet tube of the CPC was assumed to be 15 cm long, with an inner diameter of 4.5 mm, assembled horizontally. For that tube the nominal flow of the TSI 3772-CEN of 1 l/min was used. Neither the following split-up into 8 separate lines in the CPC, with 1/8 l/min flow each, nor the path from the splitting point onward, through the saturator to the condenser inlet were considered. In these tubings particle losses will occur, but the conditions inside the saturator were assumed to be too complex to operate with the PLC.

4 Results and Discussion

In the following, experimental results are presented, discussed and compared to recent literature on the topic of pressure dependent detection efficiencies of n-butanol based CPCs. Subsequently the results of the theoretical evaluations are presented and interpreted against the experimentally gained data.

4.1 Experimental Results

In this section, the experimental results for the pressure dependent measurements with the TSI 3772-CEN CPCs are presented and interpreted. For this purpose, flow rate measurements for both used CPCs (at pressure rates between 1000 hPa and 150 hPa), as well as investigated cutoff curves for the two instruments are presented first. Cutoff measurements were performed to determine the D_{50} value (for silver particles) of the utilized instruments. Subsequently follow the detection efficiency measurements for different particle diameters and pressure rates ranging from 1000 hPa to 150 hPa. The three different seed materials silver, salt and BCy are each discussed in separate subsections. Since the n-butanol fill bottles were disconnected from the instruments for all low pressure measurements (maximum three hours disconnected), it was made sure, that the TSI 3772-CEN CPCs are still able to reliably detect correct particle number concentrations over several hours of measurement time (see Appendix A). All uncertainties presented in the plots of the following sections were calculated via the instrument uncertainties (see Table 3.5) and Gaussian error propagation. For particle sizes below 100 % detection efficiency at 1000 hPa, the DMA resolution also affects the measurement uncertainties (see Figure 4.2). But since the DMA uncertainties cannot simply be transferred to the pressure dependent plots, they were not considered in sections 4.1.3, 4.1.4 and 4.1.5.

4.1.1 CPC Flow Rates

Flow rates through CPCs are important for particle number concentration calculations (subsubsection 3.1.5) and because the CPC 3772-CEN was not designed for aircraft operation, flow rates were measured at the range of pressures investigated in this study for both CPCs. The corresponding results are presented in Figure 4.1.

Measurements were performed with a TSI mass flowmeter and a pressure reducing valve (see paragraph 3.1.4.1) in front of the CPCs. At 1000 hPa, the instrument marked as CPC 1, delivered a flow rate of approximately 1.01 l/min and CPC 2 a flow rate exceeding the value of 1 l/min stated by the manufacturer (roughly 1.075 l/min). Furthermore, the flow rate was observed not to be constant for the whole pressure range. The flow rate decreased with decreasing pressure, down to around 0.93 l/min for CPC 1 and 0.98 l/min for CPC 2 at 150 hPa. Using a manufacturer preset flow rate of 1 l/min for the calculations of

particle number concentrations would lead to deviations from the actual values, thus in this study all CPC number concentrations were calculated in the way described in subsubsection 3.1.5, with the measured flow rates.
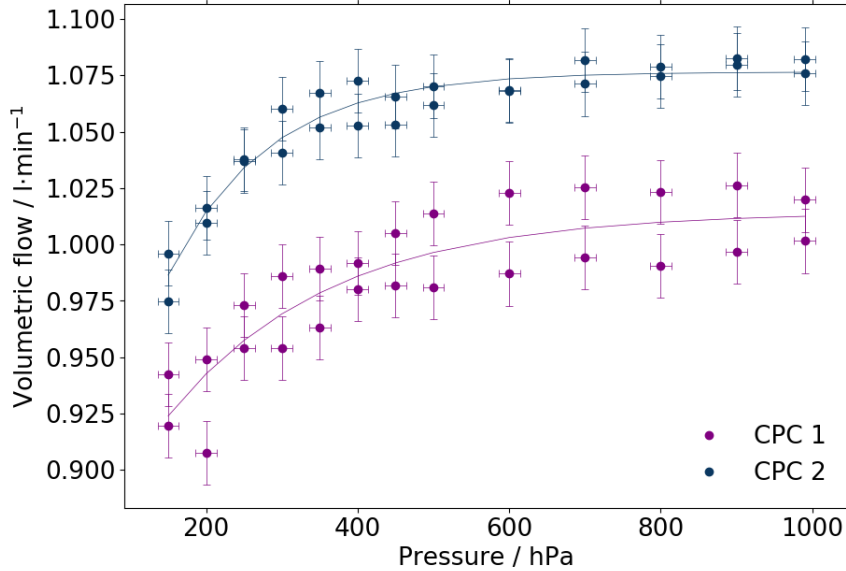
Figure 4.1: Fitted flow rates through CPCs at measurement pressure conditions, ranging from 1000 to 150 hPa. Error bars representing the instrument uncertainties (see Table 3.5).

4.1.2 Seed Material dependent CPC Cutoffs

To allow the interpretation of the pressure dependent detection efficiency measurements, cutoff curves for silver particles were determined, presented in Figure 4.2. Also included in the plots are data points for salt and BCy particles, taken from Figures 4.5 and 4.7 at 1000 hPa.

The cutoff diameter D_{50} for silver particles, determined via the curve fit functions is 6.6 ± 0.8 nm for both CPCs. This value is in agreement (within the error margins) with the D_{50} of 7 nm for silver particles given by TSI (TSI Incorporated, 2016). The data points for salt and BCy particles indicate the influence of chemical factors induced by seed particle material on the detection efficiency of n-butanol based CPCs, as elaborated by Wlasits et al. (2020). If working fluid and seed substance are of similar chemical structure, they dissolve more easily. Thereby, the rather non-polar n-butanol interacts weaker with the ionic NaCl particles, than with the less polar Ag and $C_{15}H_{24}O_x$ particles. Thus, one can expect a lower cutoff diameter for BCy and a larger D_{50} for salt particles, with respect to the cutoff curve for silver particles.
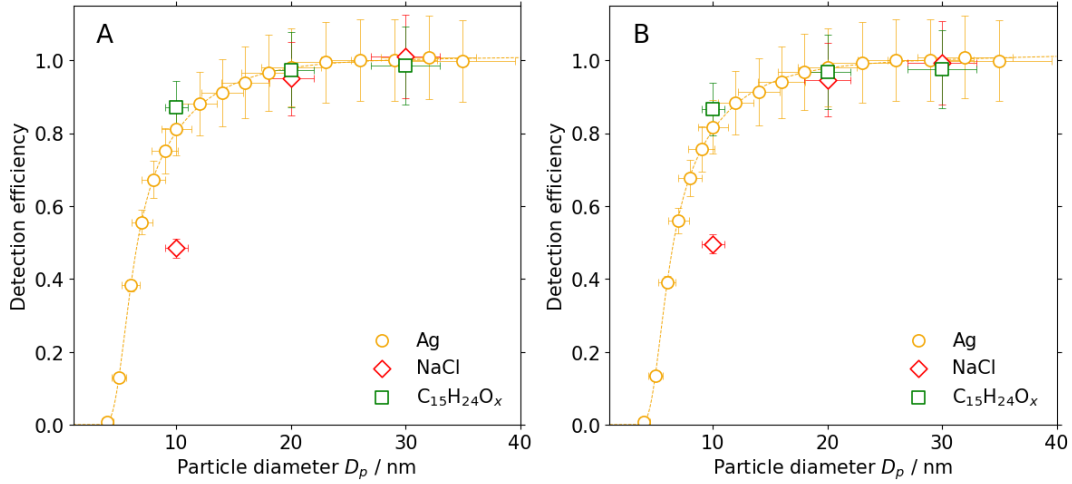
Figure 4.2: Silver particle cutoff curves for CPC 1 (A) and CPC 2 (B). For both CPCs the fit function gives a cutoff diameter D_{50} of 6.6 nm. Also included in the plots are data points for salt and BCy particles for which no complete cutoff curves were measured. These data points were taken from Figures 4.5 and 4.7 at 1000 hPa.

4.1.3 Pressure dependent Detection Efficiency for Silver Particles

Measurements with silver particles were performed for four different particle sizes, namely 7, 10, 20 and 30 nm. Larger diameters were not generated, due to temperature limitations caused by the glass tube inside the tube furnace. While the 20 and 30 nm Ag seed particles are detected in the plateau of the CPC cutoff curve (100 % detection efficiency), particles with 7 and 10 nm diameters are measured with about 60 and 80 % detection efficiency respectively, at 1000 hPa (see Figure 4.2).

The results for all measured particle diameters and both CPCs are shown in Figure 4.3. Two measurement cycles (where one cycle includes one complete detection efficiency curve for each particle size, providing information on day to day variability) are depicted, indicated by the markers in the plot, which are filled (fitted with continuous lines) for the first cycle and not filled (fitted with dashed lines) for the data of the second cycle.

The results presented here for Ag particles capture two effects. The effect of the (a) pressure dependent detection efficiency of a 3772-CEN CPC and the effect (b) of the CPC cutoff size which is also pressure dependent, however was not the specific focus of this study. It can be seen that for particles with sizes at 100 % detection efficiency at 1000 hPa the effect (a) comes into play. While for particles with sizes that are not fully counted at 1000 hPa, a combination of these two effects (a and b) comes into play.
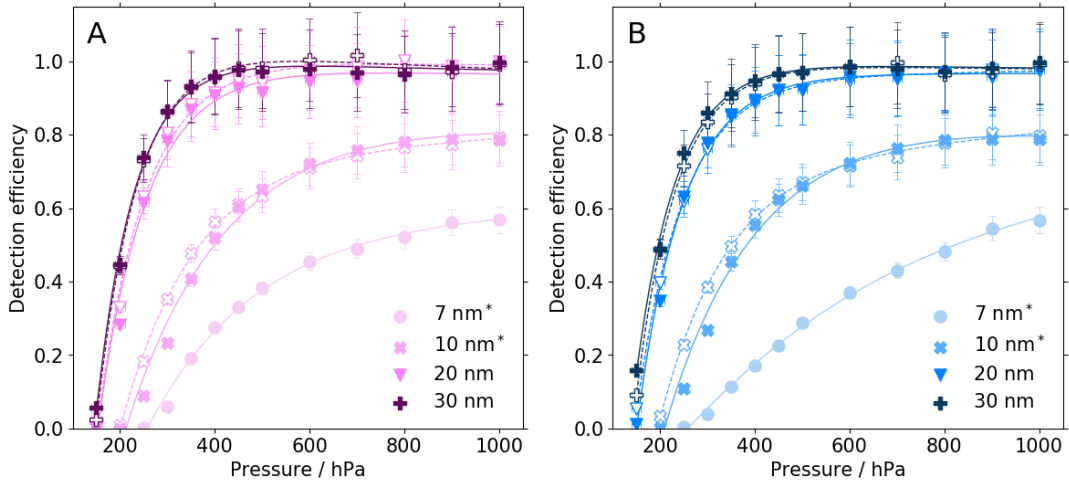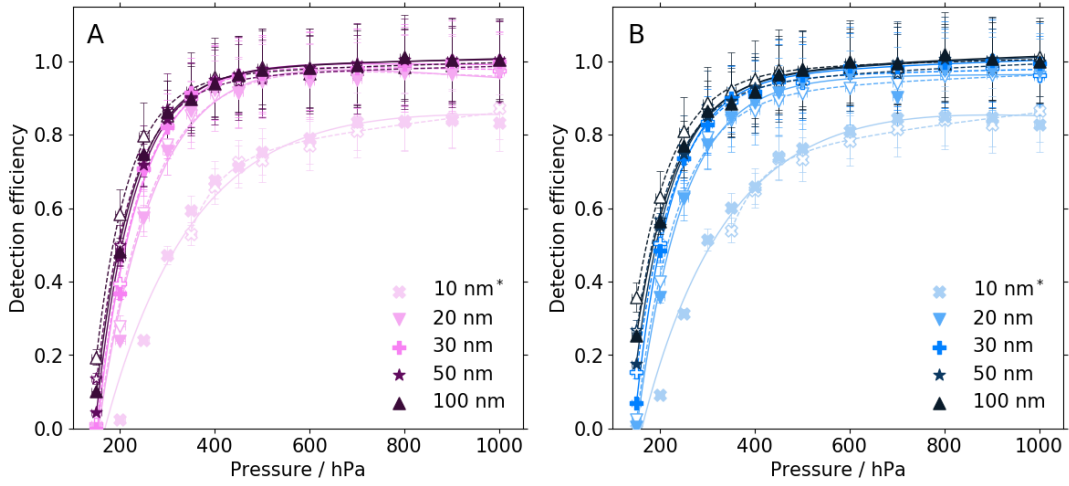
Figure 4.3: Pressure dependent detection efficiency curves of two measurement cycles, recorded on different days (markers filled and not filled respectively) for silver particles, with diameters D_p ranging from 7 nm to 30 nm. For CPC 1 (A) and CPC 2 (B). *Since only a fraction of 7 (close to cutoff size) and 10 nm particles are detected already at pressure of 1000 hPa (60 and 80 % efficiency respectively), the detection efficiency curves for these two particle sizes lie below curves for bigger particle sizes (i.e. 20 and 30 nm). This indicates that when particles are below 100 % detection of a CPC at 1000 hPa (ground level pressure) two effects come into place: the effect of particle size and pressure (in contrast to bigger sizes, where pressure is the most important factor). The curve with open markers for 7 nm particles is not included, since during that measurement, the system had to be readjusted to room pressure twice due to flow problems, which could possibly have influenced the measurement results. A plot including the second 7 nm curve can be seen in Appendix B.

As elaborated before, the cutoff size of the 3772-CEN CPC for silver particles at 1000 hPa is at 6.6 nm (50 % detection efficiency against the FCE, see Figure 4.2), thus about 60 % detection efficiency is reached for 7 nm particles in Figure 4.3 at 1000 hPa. Similarly 10 nm particles appear at about 80 % detection efficiency at 1000 hPa and in Figure 4.2 as well. This indicates that particle size will play a critical role in potential future data corrections and data interpretation. Looking at the detection efficiency curves of the 20 and 30 nm particles, it can be seen, that in the range of 1000 to 350 hPa, detection efficiencies only decrease down to a minimum value of about 90 %. Below 350 hPa, a drop in detection efficiency was detected, resulting in measured efficiencies between 28 and 49 % at 200 hPa. When comparing the fits for all measured particle sizes in Figure 4.3, it can be seen, that the curvature of the fits increases with increasing particle diameter. This behaviour even occurs when comparing the 20 and 30 nm curves, which both start off at a detection efficiency of about 100 % at 1000 hPa, although these differences lie within the uncertainty margins.

Figure 4.4 shows, that disagreements in measured number concentrations between the two CPCs arise at pressure rates below 250 hPa, where CPC 2 seems to achieve higher counting efficiencies than CPC 1. The deflection up to about 1.6 at 350 hPa for 7 nm particles, is possibly a results of inaccuracies during the measurement. Since detection efficiencies for this particle size already start at about 60 % at ambient pressure (see Figure 4.3), small differences in detection efficiencies between CPC 1 and CPC 2 have a greater influence on the relation of detection efficiencies between the two CPCs, than at higher detection efficiencies (larger particle diameters).
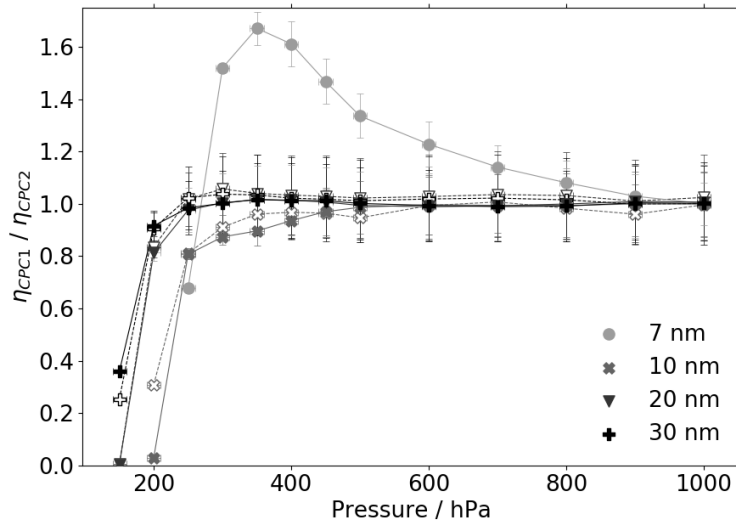
Figure 4.4: Quotient of detection efficiencies (η_{CPC1}/η_{CPC2}) for the two measurement cycles, recorded on different days (markers filled or not filled) for silver particles (with diameters D_p ranging from 7 nm to 30 nm) measured by CPC 1 and CPC 2, against pressure.

4.1.4 Pressure dependent Detection Efficiency for Sodium Chloride Particles

Salt particles of five different diameters (10, 20, 30, 50 and 100 nm) were generated and measured. Particles sized 7 nm were not included, due to the increased cutoff diameter of n-butanol based CPCs for NaCl. With NaCl particles of 10 nm diameter, about 50 % detection efficiency is reached at ambient pressure, 30, 50 and 100 nm particles are detected in the plateau of the cutoff curve (100 % detection efficiency).

The results of one measurement cycle (one detection efficiency curve for each particle diameter) is displayed in Figure 4.5. It was not possible to measure a second cycle, because flooding problems with the CPCs occurred and the particle generation setup was needed elsewhere.
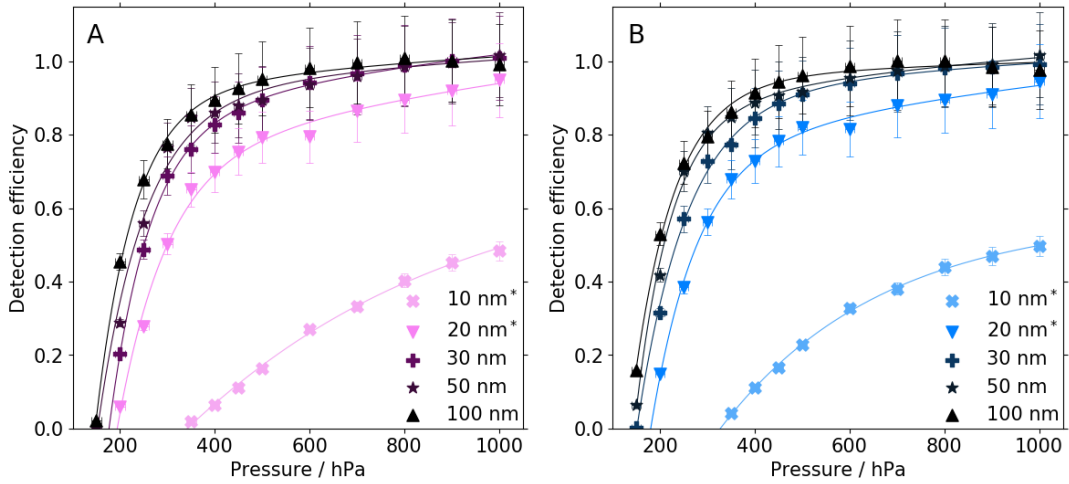
Figure 4.5: Pressure dependent detection efficiency curves for salt particles, with diameters D_p ranging from 10 nm to 100 nm. For CPC 1 (A) and CPC 2 (B). *Since only a fraction of 10 (close to cutoff size for salt) and 20 nm particles are detected already at pressure of 1000 hPa (50 and 90 % efficiency respectively), the detection efficiency curves for these two particle sizes lie below curves for bigger particle sizes (i.e. 30, 50 and 100 nm). This indicates that when particles are below 100 % detection of a CPC at 1000 hPa (ground level pressure) two effects come into place: the effect of particle size and pressure (in contrast to bigger sizes, where pressure is the most important factor).

Apart from the differences, caused by the seed particle material (such as the increased cutoff diameter at 1000 hPa), characteristics similar to the ones discussed in subsubsection 4.1.3 are distinguishable. The results for particle diameters of 10 and 20 nm again capture the two effects of (a) pressure dependent detection efficiency and the (b) effect of the CPC cutoff size, described in the previous section. The detection efficiencies of the 30, 50 and 100 nm particles only decrease down to a minimum value of about 90 % within the range of 1000 to 500 hPa. At 350 hPa, detection efficiencies of these three particle sizes vary between 75 and 85 %. Below 350 hPa, again a drop in detection efficiency can be seen, resulting in measured efficiencies of 20-53 % at 200 hPa. As observed for silver particles, the curvature of the detection efficiency curve fits, becomes more pronounced with increasing particle diameter. Within the boundaries of uncertainties, this trend also seems to resume for 30, 50 and 100 nm.

Differences in detection efficiency between the two CPCs (see Figure 4.6) occur in a fashion, likewise to subsubsection 4.1.3, where higher detection efficiencies are obtained by CPC 2 in the pressure range below about 250 hPa. The deviations for 10 nm particles, where the differences already appear way above 250 hPa, probably arise due to the same circumstances, elaborated in the previous chapter for 7 nm silver particles.
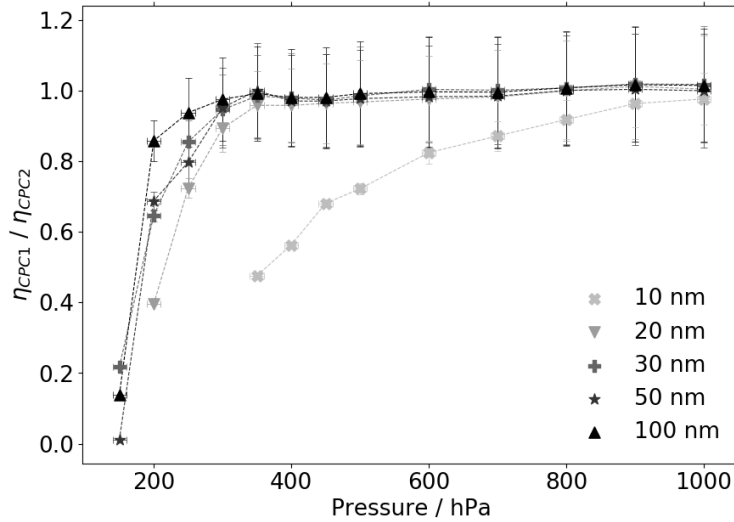
Figure 4.6: Quotient of detection efficiencies (η_{CPC1}/η_{CPC2}) for silver particles (with diameters D_p ranging from 10 nm to 100 nm) measured by CPC 1 and CPC 2, against pressure.

4.1.5 Pressure dependent Detection Efficiency for Beta Caryophyllene Particles

BCy measurements were also performed for particle diameters of 10, 20, 30, 50 and 100 nm. For this species, generation of smaller particles in sufficient number concentration was not feasible, which was caused by limitations of the reaction path inside the flow tube. Figure 4.7 shows the respective results for two measurement cycles (where one cycle includes one complete detection efficiency curve for each particle size), which are indicated by the markers in the plot, where filled markers (fitted with continuous lines) represent the first cycle and unfilled markers (fitted with dashed lines) the data of the second cycle.

The measurement outcomes for BCy appear to be very similar to those presented for silver in subsubsection 4.1.3. The results for particle diameters of 10 nm again capture the two effects of (a) pressure dependent detection efficiency and the (b) effect of the CPC cutoff size, described in subsubsection 4.1.3. The detection efficiencies of the 20, 30, 50 and 100 nm particles only decrease down to values between 85 and 92 % within the range between 1000 and 350 hPa. Below 350 hPa, again a drop in detection efficiency can be seen, resulting in measured efficiencies of 26-63 % at 200 hPa. In alignment with both other seed particle species, the development of the fit curvature with increasing particle diameter, up to 100 nm can also be seen in the BCy data.

Again CPC 2 was reporting higher detection efficiencies than CPC 1 (see Figure 4.8) at pressure levels lower than about 250 hPa. Thereby the data gained for BCy is in compliance with the results for silver and salt particles.

Figure 4.7: Pressure dependent detection efficiency curves of two measurement cycles, recorded on different days (markers filled and not filled respectively) for BCy particles, with diameters D_p ranging from 10 nm to 100 nm. For CPC 1 (A) and CPC 2 (B). *Since only a fraction of 10 nm particles are detected already at pressure of 1000 hPa (85 % efficiency respectively), the detection efficiency curves for this particle size lies below curves for bigger particle sizes (i.e. 20, 30, 50 and 100 nm). This indicates that when particles are below 100 % detection of a CPC at 1000 hPa (ground level pressure) two effects come into place: the effect of particle size and pressure (in contrast to bigger sizes, where pressure is the most important factor).
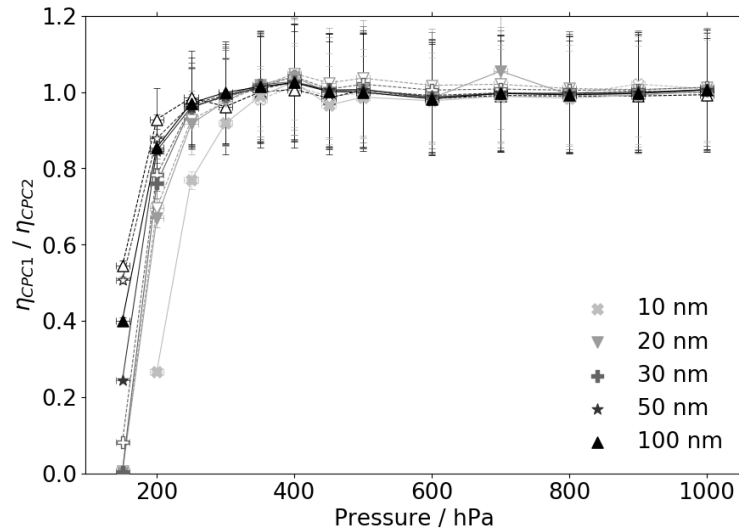
Figure 4.8: Quotient of detection efficiencies (η_{CPC1}/η_{CPC2}) for the two measurement cycles, recorded on different days (markers filled or not filled) for BCy particles (with diameters D_p ranging from 10 nm to 100 nm) measured by CPC 1 and CPC 2, against pressure.

4.1.6   Comparison between Particle Species

Figure 4.9 displays the correspondent detection efficiency curves for silver, salt and BCy particles (of the first cycle respectively, if two cycles were measured), with a diameter of 10 nm (left plot) and 30 nm (plot on the right hand side), for pressure rates ranging from 1000 hPa to 150 hPa.
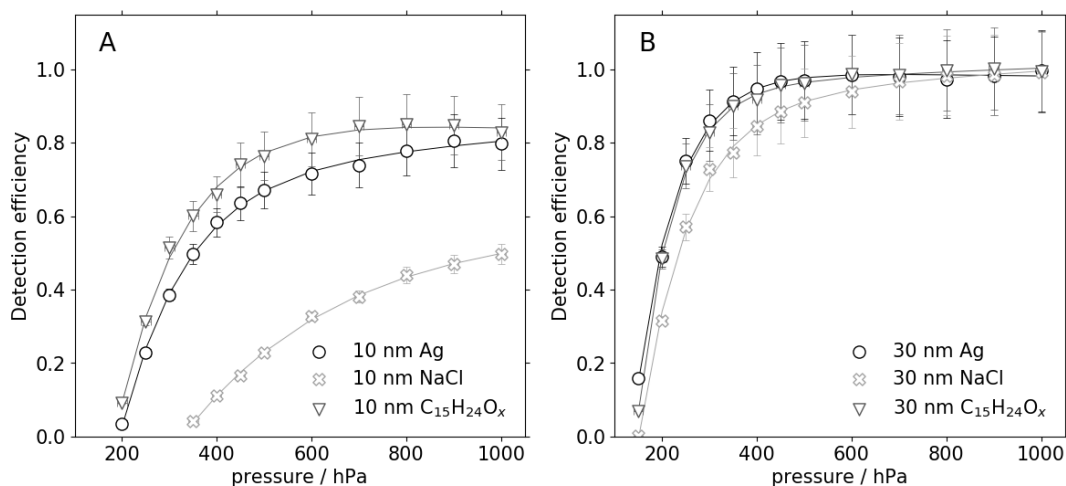
Figure 4.9: Pressure dependent detection efficiency curves of silver, salt and BCy particles, measured with CPC 2. With particle diameters of 10 nm (A) and 30 nm (B). Uncertainties were calculated via the instrument uncertainties and Gaussian error propagation.

Plot B on the left hand side of Figure 4.9 captures both the effect of the the cutoff size of the CPC and the effect of seed particle material, which has an impact on the first mentioned (see subsubsection 4.1.2, 10 nm Ag and BCy at about 80 % detection efficiency and 10 nm NaCl at 50 % efficiency at 1000 hPa). This means that CPC counts only a fraction of particles with 10 nm and these three particle material, indicating that both the composition of particles and sizes need to be taken into account when using CPC 3772-CEN on an aircraft. The third effect seen here is the effect of pressure, leading to the decrease in detection efficiency with decreasing pressure. However, for particle sizes detected at maximum efficiency by the TSI 3772-CEN CPC (Figure 4.9 B), the effect of pressure can be seen under less influence of particle composition.

4.1.7   Comparison to recent Studies

The outcomes of this study are in agreement with the findings presented by Zhang and Liu (1991) and Takegawa and Sakurai (2011), regarding the cutoff-shift to lager particle diameters with decreasing pressure, contrary to the results of Hermann and Wiedensohler (2001). A comparison of the findings of Zhang and Liu (1991), Takegawa and Sakurai (2011) and the results of this work is presented in Figure 4.10.
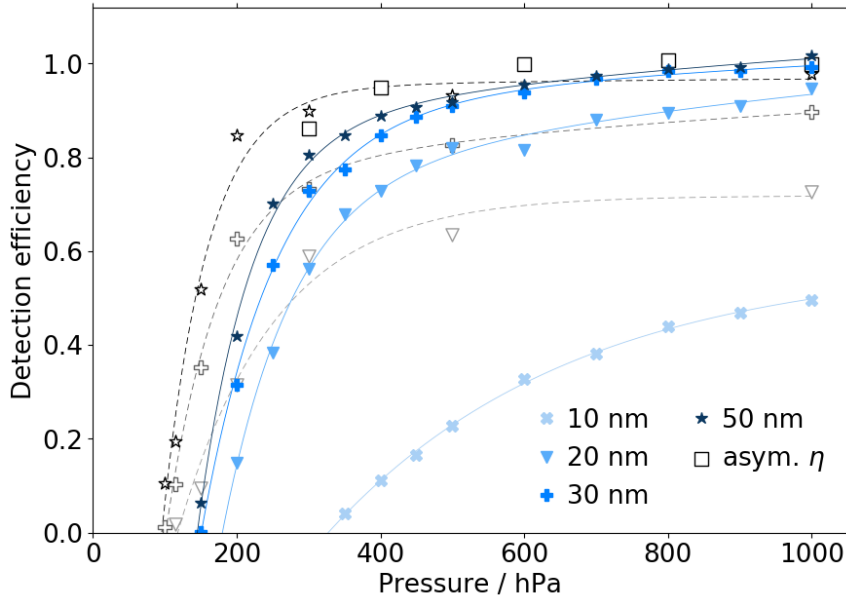
Figure 4.10: Pressure dependent detection efficiency curves for NaCl particles. Filled blue markers represent data from this study and open markers represent Zhang and Liu (1991) and correspond to the same particle sizes and material. The open square markers depict the asymptotic detection efficiencies, measured by Takegawa and Sakurai (2011) for sucrose particles with a TSI 3771 CPC down to 300 hPa. Error bars were not included to ensure readability.

The drop in detection efficiency at low pressure rates reported by Zhang and Liu (who used the butanol based TSI 3760 CPC, with a nominal D_{50} of about 12.3 nm for silver particles (Wiedensohlet et al., 1997)) was also found in the course of this thesis. The measurements are in good agreement, although Zhang and Liu achieved a lower minimum pressure of 100 hPa, instead of 150 hPa. For 50 nm particles, the difference in detection efficiency at 150 hPa is 45 % between the corresponding data point published by Zhang and Liu (1991) and the data measured in this study. Working with a TSI 3771 CPC (with a D_{50} of 10 nm) Takegawa and Sakurai report a significant decrease of asymptotic detection efficiency (i.e. detection efficiency at plateau level of the cutoff curve) at 300 hPa, the lowest pressure level presented by them (see Figure 4.10). This decrease in asymptotic (or maximum) detection efficiency with decreasing pressure observed by Takegawa and Sakurai (2011), was also reported by Zhang and Liu (1991) and Hermann and Wiedensohler (2001) and can also be seen in the results of this work. A major difference to previous studies is the investigation of multiple particle species, allowing inter-comparison between different seed materials and consistency check between two same CPC models. As far as is known, this study is also the first to examine TSI 3772-CEN CPCs under varying pressure conditions.

4.2 Theoretical Results

The results of the theoretical evaluations, including simulations of condenser supersaturation profiles, activation efficiency curves, diffusion losses and pressure dependent detection efficiency curves are presented in the following section. In addition, the theoretical results are compared with the experimentally obtained results.

4.2.1 Supersaturation Profiles
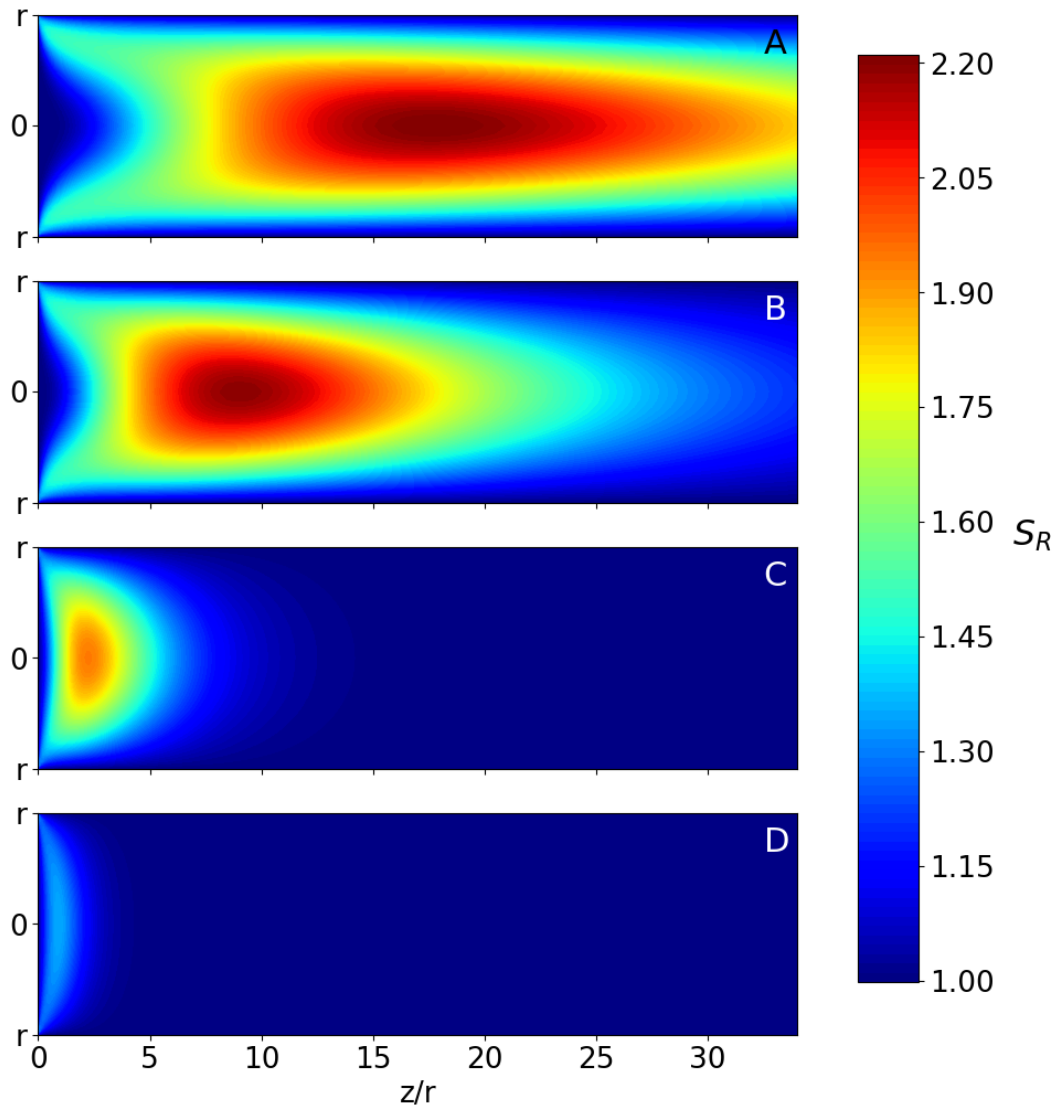
Figure 4.11: Simulated supersaturation profiles inside the condenser tube of the TSI 3772-CEN at 1000 hPa (A), 500 hPa (B), 100 hPa (C) and 10 hPa (D) ambient pressure. With the radius r and the dimensionless length z/r of the tube. The color coding shows the supersaturation distribution inside the tube.

By solving Equation 3.15 separately for both transfer mechanisms, the correspondent profiles were calculated (see Appendix C). Combining these profiles by means of Equation 2.3, the saturation ratio for every point on the simulation mesh was calculated, resulting in supersaturation profiles, displayed in Figure 4.11. The results for four representative pressure levels (1000, 500, 100 and 10 hPa) are depicted.

4.2.2 Activation Efficiencies
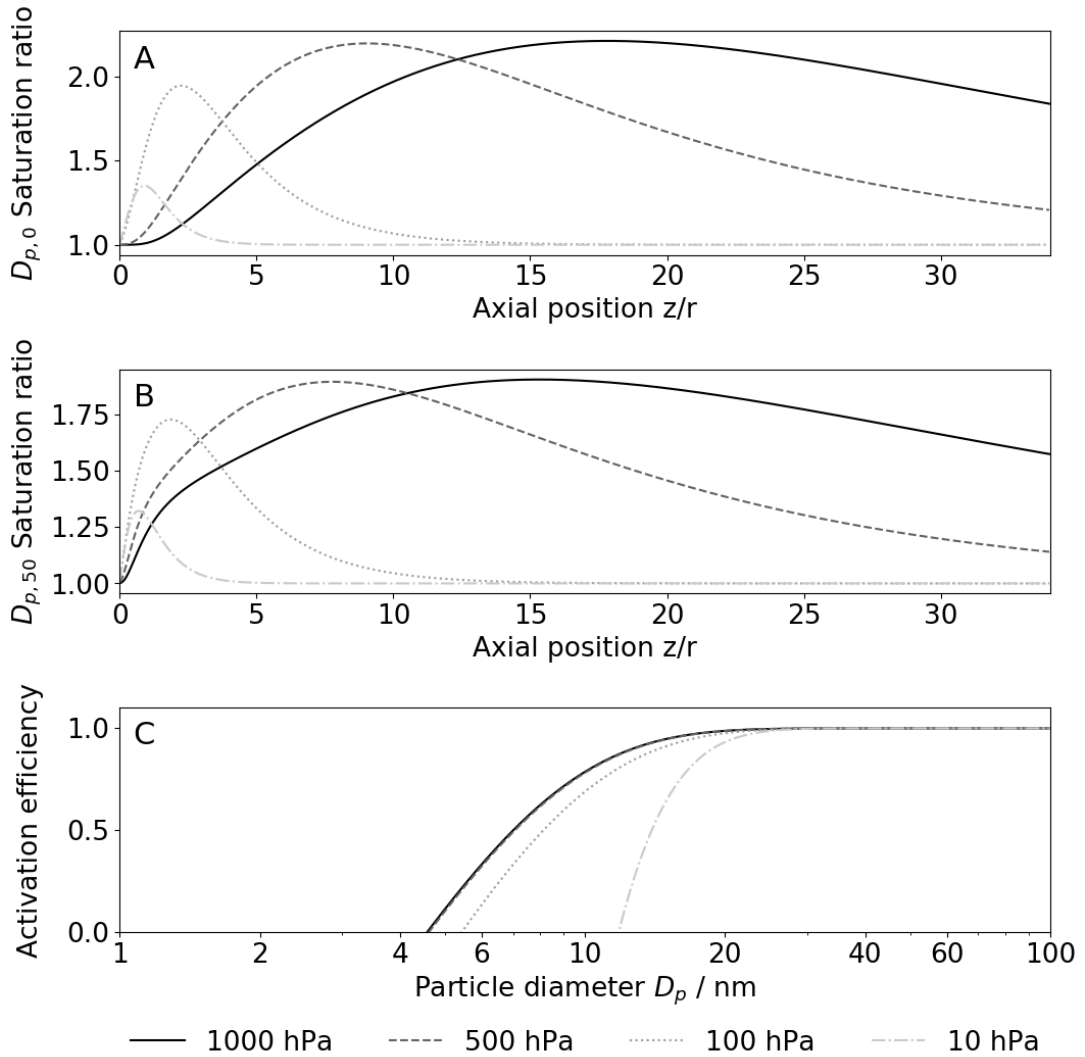
Figure 4.12: Theoretical calculations, based on the simulations. The centerline (r=0) saturation ratio along z/r inside the condenser tube (A). The saturation ratio at r/2 along z/r (B), as well as the resulting activation efficiencies for the four representative pressure levels ranging from 1000 hPa to 10 hPa (C). Losses induced by penetration and diffusion were not considered in (C).

In Figure 4.12 the axial saturation ratios at r=0 and r/2 (referring to Figure 4.11), as well es the resulting activation efficiencies (calculated with Equation 3.21), for the 4 representative ambient pressure levels are shown.
In Figures 4.11 and 4.12 it can be seen, that a decrease in pressure leads to a shift of the area of highest supersaturation towards the condenser entrance. Also the value of maximum S_R reduces with p, which leads to a shift of the cutoff diameter to larger sizes (see Figure 4.12 C).

To verify the conformity between theoretical and experimental data, the measured detection efficiency curves of both CPCs and the correspondent simulation results at 1000 hPa are depicted in Figure 4.13. As can be seen, a good agreement within the uncertainty margins of the experimental results was achieved (for more data at various condenser temperature settings see Appendix C). Moreover, the cutoff diameter of the calculated curve equals to 7 nm, which is in compliance with the nominal value given by TSI Incorporated (2016).
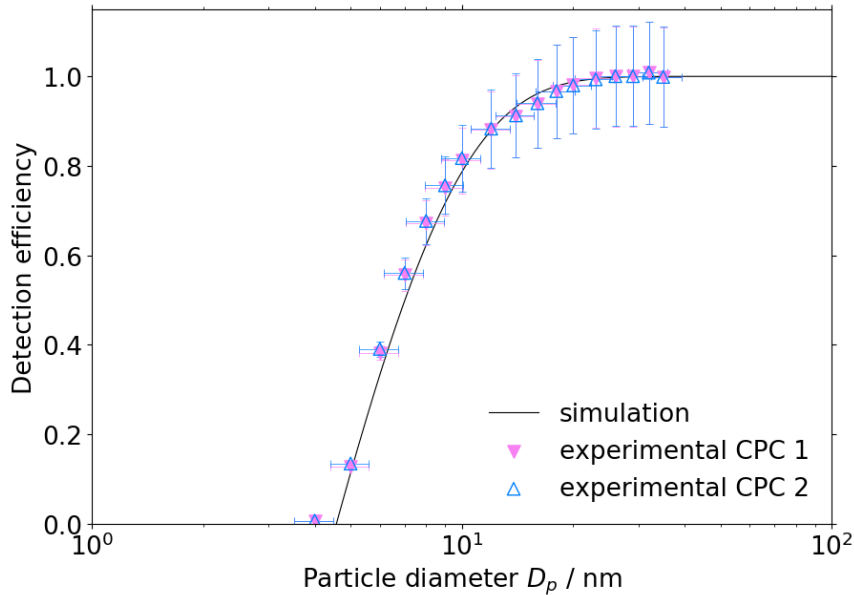
Figure 4.13: Experimental (for silver particles) and theoretical detection efficiency of the TSI 3772-CEN at 1000 hPa.

4.2.3 Diffusion Losses

The computations for diffusion losses inside the TSI 3772-CEN aerosol inlet tube were performed for pressure rates ranging from 1000 hPa to 10 hPa.

Looking at the four exemplary graphs in Figure 4.14, it can be seen, that the transmission efficiency (or sampling efficiency, referring to Equation 3.5) decreases at low pressure rates, due to diffusion losses. The decrease even increases with decreasing pressure.
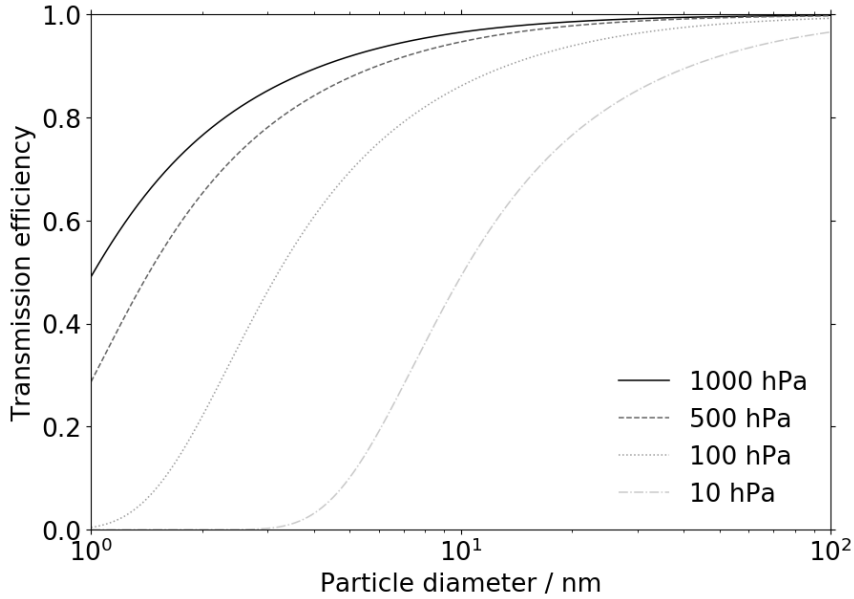
Figure 4.14: Diffusion losses inside the TSI 3772-CEN CPC, for 4 exemplary pressure levels (1000, 500, 100 and 10 hPa), derived with the particle loss calculator (Weiden et al., 2009).

4.2.4 Pressure Dependent Detection Efficiency Curves

For a further comparison of the simulation results with the experimental data presented in section 4, a similar plot of pressure dependent detection efficiencies for fixed particle sizes was created, with pressure on the x-axis and detection efficiency on the y-axis. To achieve this goal, cutoff plots as they are displayed in Figure 4.12 were created for 15 pressure levels between 10 and 1000 hPa. Activation efficiencies at each particle size (7, 10, 20, 30, 50 and 100 nm) were evaluated respectively. Transmission efficiencies, calculated with the particle loss calculator (see Figure 4.14) for the 15 pressure levels between 10 and 1000 hPa were taken into consideration by multiplying the respective values at the fixed particle sizes (7, 10, 20, 30, 50 and 100 nm) with the activation efficiencies. Figure 4.15 shows the resulting detection efficiencies, the dashed lines illustrate the activation efficiencies not including diffusion losses and the continuous lines display the combination of activation efficiencies and transmission efficiencies (diffusion losses).

When looking at the activation efficiencies (without diffusion losses) in Figure 4.15, no significant decrease in counting efficiency is noticeable down to 150 hPa for fixed particle sizes, the minimum pressure level for experimental results. Thereby, the dependency of the fit function curvature on the particle diameter is not as distinct as in the measurement results. For D_p bigger than 30 nm, no changes in activation efficiency arise with varying pressure, at all. The additional consideration of diffusion losses results in a more distinct separation

between particle sizes, up to diameters of 100 nm. This general trend, as well as the increasing curvature of the graphs with increasing particle diameter, is in conformity with the measurement data.
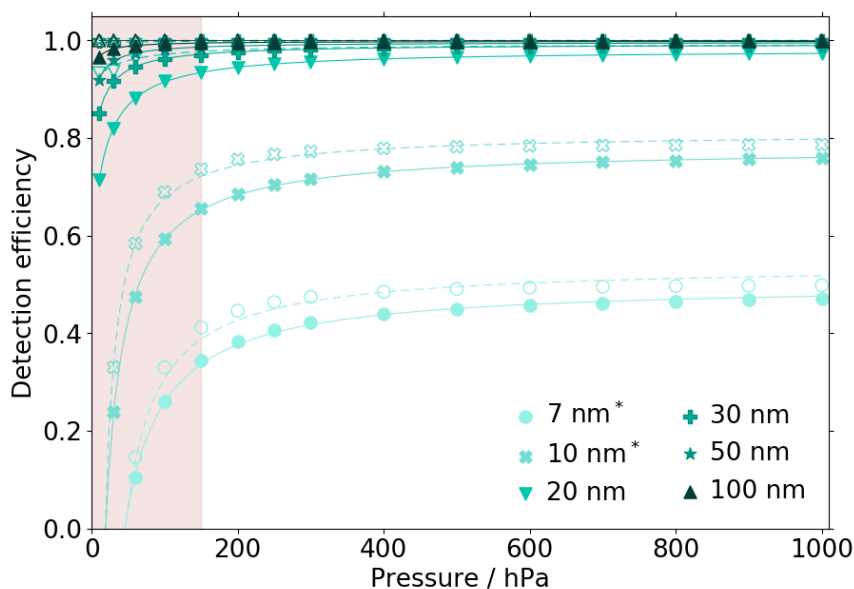
Figure 4.15: The dashed lines depict the theoretical detection efficiencies from the simulations, while the continuous lines also include diffusion losses. For ambient pressure ranging from 1000 hPa to 10 hPa, for particle sizes between 7 nm and 30 nm. *Since only a fraction of 7 (close to cutoff size) and 10 nm particles are detected already at pressure of 1000 hPa (0.5 and 0.8 efficiency respectively), the detection efficiency curves for these two particle sizes lie below curves for bigger particle sizes (i.e. 20 nm and larger, see subsubsection 4.1.3). The area highlighted in red, marks the range in which no measurement data was producible, since detection efficiencies were equal to 0.

The comparison between theoretical and experimental findings displayed in Figure 4.16 shows that the consideration of diffusion losses is not enough to fully explain the experimental results and suggests that additional particle loss mechanisms within the CPCs may dominate the counting efficiency at pressure levels below 350 hPa. As already elaborated by Zhang and Liu (1990) various factors, other than diffusion losses may have an impact on the CPCs performance at low pressure conditions, like Stefan flow or thermophoretic and diffusiophoretic effects. Also the aerosol flow carrying the droplets grown inside the condenser could experience significant transport losses, with decreasing pressure on its way to the optics. Hermann and Wiedensohler (2001) performed low pressure measurements with a TSI 3760 CPC, they mention that at low pressure rates, the aerosol flow focusing by the nozzle at the optics entrance may not work properly, so that not all particles are detected. However, Takegawa and Sakurai

(2011) argued that the nozzle may not be the explanation for reduced detection efficiency at low pressure rates, after they conducted a pulse height analysis with a TSI 3771 CPC. Following that analysis, Takegawa and Sakurai (2011) conclude that a reduction of the saturation ratio with decreasing pressure in the condenser of the CPC may be the cause for the reduced detection efficiency at low pressure rates. The simulation data of the condenser supersaturation profiles obtained within this thesis do not result in the experimentally observed detection efficiency drop in the range of 150 to 350 hPa. Thus, changes of the supersaturation profiles with pressure may not be the cause for the observed decrease in detection efficiency, although unknown effects at reduced pressure rates could possibly influence the saturation in the condenser. Furthermore, unknown effects at the pressure reducing valve, could play into the measurement results (as Hermann and Wiedensohler (2001) also mentioned). At low pressure rates, when the opening of the valve is small, charge transfers between particles could possibly occur additionally to particle losses, altering the comparison of CPC and FCE number concentrations.
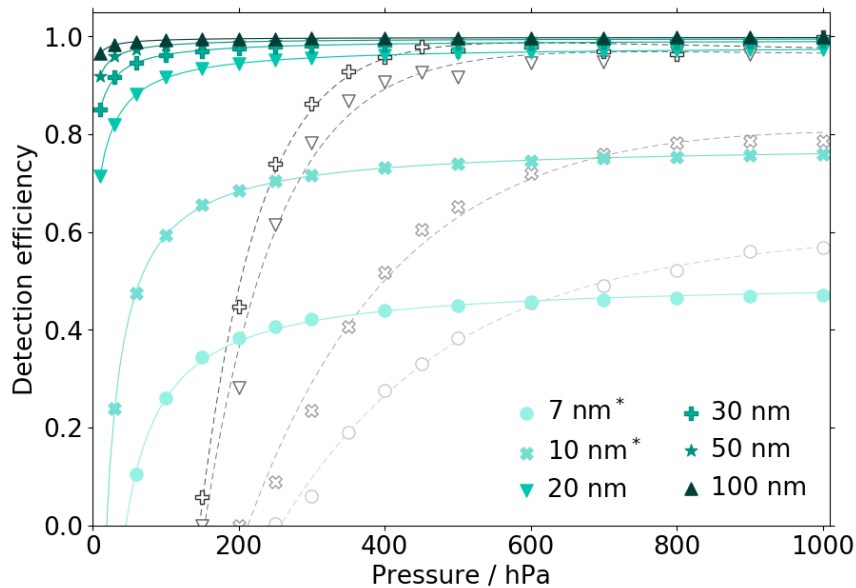
Figure 4.16: Theoretical detection efficiencies (turquoise lines) and experimental detection efficiencies for Ag particles (dashed, grey lines, CPC 1) against pressure, for particle sizes between 7 nm and 30 nm. *Since only a fraction of 7 (close to cutoff size) and 10 nm particles are detected already at pressure of 1000 hPa (0.5 or 0.6 and 0.8 efficiency respectively), the detection efficiency curves for these two particle sizes lie below curves for bigger particle sizes (i.e. 20 nm and larger, see subsubsection 4.1.3). Error bars were not plotted for the experimental data points to ensure readability.

5 Conclusion

This research work aimed to examine the dependence of the detection efficiency of two conductive cooling type n-butanol-based TSI 3772-CEN CPCs on pressure levels representative for airborne measurement campaigns. The range of pressures explored experimentally and theoretically varied between 150 and 1000 hPa and 10 and 1000 hPa, respectively.

In the experimental part, three different particle types such as silver, Sodium Chloride and Beta Caryophyllene were used, considering the dependency of a CPC response to the particle material. Two 3772-CEN CPCs were used to allow for a consistency check between same CPC models. Reproducible experimental results were obtained for these instruments (with repeated measurements on different days) and compared to recent literature.

Seed particle material is an important factor, regarding CPC measurements, since it influences the cutoff size of the instrument. The cutoff diameter of the TSI 3772-CEN CPC was determined experimentally (6.6 $\pm$ 0.8 nm) and theoretically (7 nm) for silver particles at ground level pressure conditions (1000 hPa). The results are in agreement with the specifications by the manufacturer (TSI Incorporated, 2016). Recent studies (such as Wlasits et al. (2020), Tauber et al. (2019) or Kangasluoma1 et al. (2014)) investigated the seed material dependence of n-butanol based CPCs. Wlasits et al. (2020) observed a lower cutoff diameter for BCy and a larger D_{50} for NaCl particles, with respect to the cutoff curve for silver particles. Although this study did not investigate the cutoff size for BCy and NaCl seed material, the shift of the cutoff size to bigger sizes for NaCl at ambient pressure was also observed in this work.

At measurement conditions below ambient pressure, the TSI 3772-CEN CPCs were operated without the working fluid supply bottles in order to avoid flooding of the CPCs with n-butanol. It was assured, however, that the respective wicks are wetted and that the performance of the CPCs was not affected. Because the CPC 3772-CEN was not specifically designed for aircraft operation, the volumetric flow rate, which is used to calculate the particle number concentration, was also investigated as a function of pressure. A slight decrease in volumetric flow rate was found (about 10 % reduction at 150 hPa). The measured flow rates were used in particle number concentration calculations.

This study captured two pressure related effects that need to be carefully considered when operating a TSI 3772-CEN CPC (or any other CPC) on an aircraft. The effect of the pressure on particle detection efficiency, and the effect of the cutoff diameter D_{50}, which is also pressure dependent. The latter however was not the specific focus of this study.

The diameter of the particles sampled by CPCs plays a critical role in the interpretation of the detection efficiency curves at various pressure conditions. When the TSI 3772-CEN CPC samples particles at sizes that are too small to be counted at 100 % efficiency at ground level pressure conditions (such as 7 and 10 nm Ag), at low pressure conditions a combination of the effects of pressure and cutoff diameter on detection efficiency takes place leading to a more challenging data correction and interpretation. The effect of the decreasing pressure is clearly visible for all particles with 100 % detection efficiency at 1000 hPa, i.e. for all particle types with Dp > 10 nm used here. For silver particles with diameter > 10 nm (100 % detection efficiency at 1000 hPa), a gradual decrease of detection efficiency, by approximately from 100 % to about 90 % was observed for the pressure range between 1000 and 350 hPa. At 200 hPa, the detection efficiency was between 28 % and 49 %. A similar result was obtained for BCy particles with D_p > 10 nm, where detection efficiency decreased to a minimum of 85 % at 350 hPa. At 200 hPa, detection efficiencies between 26 % and 63 % were observed. For NaCl particles > 20 nm, a gradual decrease to 75-85 % detection efficiency was recorded between 1000 and 350 hPa. At 200 hPa, detection efficiencies varied between 20 % and 53 % for this particle material. A similar decrease in detection efficiency at low pressure has been observed previously by Zhang and Liu (1991) and Takegawa and Sakurai (2011), both investigating n-butanol based CPCs. In these two studies, a shift of the cutoff diameter to larger sizes, with decreasing pressure is reported. A similar trend was observed for all particle material studied here, but in order to quantify the shift, cutoff measurements at various pressure stages would be necessary, which was beyond the focus of this study.

Complementary theoretical analysis was undertaken, for the construction of pressure dependent, theoretical detection efficiency curves (for spherical, insoluble seed particles, with respect to n-butanol). This involved carrying out simulations of the supersaturation profiles inside the instruments condenser, by numerically solving the heat and mass transfer equations. The results of these theoretical assessments are in good agreement with the measurement data at 1000 hPa. However, the strong decrease in detection efficiency occurred at lower pressure levels (below 150 hPa, instead of 350 hPa), requiring additional mechanisms to explain the experimentally obtained data. For this reason, diffusion losses within the instruments were also taken into account. This led to more consistent theoretical results, when compared to the measurement data. However, correcting for losses did not explain the difference between the theoretical and experimental results at pressure rates below 350 hPa. Similar discrepancies between simulations and experimentally obtained data were also found by Zhang and Liu (1991). Further deliberations are necessary for a complete description of the processes taking place inside the CPCs at low pressure. Perhaps, the reason for the decreasing detection efficiency at pressure levels below 350 hPa could be internal particle losses in the CPCs used in this study. According to

Hermann and Wiedensohler (2001), unknown effects, such as charge exchanges at the pressure reducing valve, could possibly occur at low pressure levels (small opening diameter of the valve) and thereby alter the comparison of CPC and FCE number concentrations. A future task could be to find out, how nano-particles are influenced when passed through a pressure reducing valve. One way to reach this goal is by subsequent analysis of the particles with a mass spectrometer (e.g. Ionicons "Atmospheric Pressure Interface Time-of-Flight" (APi-TOF) mass spectrometer) in order to find out more about the mass to charge ratio.

The results of this study underline the importance of carrying out thorough laboratory evaluations on each individual CPC before its use in aircraft-based campaigns. Although identical CPC models were used in this study, small differences in detection efficiencies at pressure rates below 250 hPa were found between two TSI 3772-CEN devices, suggesting that small constructional differences may have an impact under these conditions.

The results point out the need to consider both, the size and the pressure dependence of the detection efficiency of a 3772-CEN CPC when interpreting aircraft-based data. Another method to minimize pressure-dependent effects during airborne CPC measurements would be the use of a constant pressure inlet, such as described by Williamson et al. (2018), but also in this case particle losses at the constant pressure inlet need to be considered.

References

Agarwal, J. K. and Sem, G. J. (1980), 'Continuous flow, single-particle-counting condensation nucleus counter', *Aerosol Science* **11**(4), 343–357. DOI: `https://doi.org/10.1016/0021-8502(80)90042-7`.

Andreae, M. O., Afchine, A., Albrecht, R., Holanda, B. A., Artaxo, P., Barbosa, H. M. J., Borrmann, S., Cecchini, M. A., Costa, A., Dollner, M., Fütterer, D., Järvinen, E., Jurkat, T., Klimach, T., Konemann, T., Knote, C., Krämer, M., Krisna, T., Machado, L. A. T., Mertes, S., Minikin, A., Pöhlker, C., Pöhlker, M. L., Pöschl, U., Rosenfeld, D., Sauer, D., Schlager, H., Schnaiter, M., Schneider, J., Schulz, C., Spanu, A., Sperling, V. B., Voigt, C., Walser, A., Wang, J., Weinzierl, B., Wendisch, M., and Ziereis, H. (2018), 'Aerosol characteristics and particle production in the upper troposphere over the amazon basin', *Atmos. Chem. Phys.* **18**, 921–961. DOI: `https://doi.org/10.5194/acp-18-921-2018`.

Andreae, M. and Rosenfeld, D. (2008), 'Aerosol–cloud–precipitation interactions. Part 1. The nature and sources of cloud-active aerosols', *Earth-Science Reviews* **89**, 13–41.

Boucher, O., Randall, D., Artaxo, P., Bretherton, C., Feingold, G., Forster, P., Kerminen, V.-M., Kondo, Y., Liao, H., Lohmann, U., Rasch, P., Satheesh, S., Sherwood, S., Stevens, B. and Zhang, X. (2013), *Clouds and Aerosols. In: Climate Change 2013: The Physical Science Basis. Contribution of Working Group I to the Fifth Assessment Report of the Intergovernmental Panel on Climate Change.*, United Kingdom and New York: Cambridge University Press.

Bricard, J., Delattre, P., Madelaine, G. and Pourprix, M. (1976), Detection of ultra-fine particles by means of a continuous flux condensation nuclei counter, *in* 'Fine Particles: Aerosol Generation, Measurement, Sampling, and Analysis', New York, Academic Press, New York, pp. 565–580. edited by B. Y. H. Liu.

Davies, C. N. (1978), 'Evaporation of airborne droplets', *Fundamentals of Aerosol Science* . Wiley, New York.

DDBST, Dortmund Data Bank (DDB) (n.d.), 'Saturated Vapor Pressure', `http://ddbonline.ddbst.de/AntoineCalculation/AntoineCalculationCGI.exe`. Accessed: Apr. 06. 2020.

Flagan, R. C. (1999), 'On differential mobility analyzer resolution', *Aerosol Sci. Tech.* **30**(6), 556–570. DOI: `https://doi.org/10.1080/027868299304417`.

Flagan, R. C. (2010), 'On differential mobility analyzer resolution', *Aerosol Sci. Tech.* **30**(6), 556–570. DOI: `https://doi.org/10.1080/027868299304417`.

Fletcher, N. H. (1958), 'Size effect in heterogeneous nucleation', *Chem. Phys.* **29**, 572–576. DOI: `https://doi.org/10.1063/1.1744540`.

Fuchs, N. (1963), 'On the stationary charge distribution on aerosol particles in a bipolar ionic atmosphere', *Geofisica Pura e Applicata* **56**(1), 185–193. DOI: `https://doi.org/10.1007/BF01993343`.

Hallquist, M., Wenger, J. C., Baltensperger, U., Rudich, Y., Simpson, D., Claeys, M., Dommen, J., Donahue, N. M., George, C., Goldstein, A. H., Hamilton, J. F., Herrmann, H., Hoffmann, T., Iinuma, Y., Jang, M., Jenkin, M. E., Jimenez, J. L., Kiendler-Scharr, A., Maenhaut, W., McFiggans, G., Mentel, T. F., Monod, A., Prevot, A. S. H., Seinfeld, J. H., Surratt, J. D., Szmigielski, R. and Wildt, J. (2009), 'The formation, properties and

impact of secondary organic aerosol: current and emerging issues', *Atmos. Chem. Phys.* **9**, 5155—-5236. DOI: `https://doi.org/10.5194/acp-9-5155-2009`.

Hearn, J. D., Lovett, A. J. and Smith, G. D. (2005), 'Ozonolysis of oleic acid particles: evidence for a surface reaction and secondary reactions involving criegee intermediates', *Phys. Chem. Chem. Phys.* **7**, 501–511. DOI: `https://doi.org/10.1039/B414472D`.

Hering, S. V., Lewis, G. S., Spielman, S. R., Eiguren-Fernandez, A., Kreisberg, N. M., Kuang, C. and Attoui, M. (2017), 'Detection near 1-nm with a laminar-flow, water-based condensation particle counter', *Aerosol Sci Tech* **51**(3), 354–362. DOI: `http://dx.doi.org/10.1080/02786826.2016.1262531`.

Hermann, M., Wehner, B., Bischof, O., Han, H. S., Krinke, T., Liu, W., Zerrath, A. and Wiedensohler, A. (2007), 'Particle counting efficiencies of new tsi condensation particle counters', *Aerosol Science* **38**(6), 674–682. DOI: `https://doi.org/10.1016/j.jaerosci.2007.05.001`.

Hermann, M. and Wiedensohler, A. (2001), 'Counting effciency of condensation particle counters at low-pressures with illustrative data from the upper troposphere', *Aerosol Science* **32**, 975–991.

Hienola, A. I., Vehkamäki, H., Lauri, A., Wagner, P. E., Winkler, P. M. and Kulmala, M. (2007), 'The first heterogeneous nucleation theorem including line tension: Analysis of experimental data', *O'Dowd C.D., Wagner P.E. (eds) Nucleation and Atmospheric Aerosols. Springer, Dordrecht* . Springer, Dordrecht. DOI: `https://doi.org/10.1007/978-1-4020-6475-3_48`.

Hinds, W. C. (1999), *Aerosol technology: properties, behavior, and measurement of airborne particles. Second Edition.*, New York:John Wiley and Sons, Inc.

Holl, W. and Mühleisen, R. (1955), 'A new condensation nuclei counter with continuous oversaturation', *Geofis. Pura Appl.* **31**(1), 21–25. DOI: `https://doi.org/10.1007/BF01999579`.

Holman, J. P. (1972), *Heat Transfer*, New York: McGraw-Hill. DOI: `https://doi.org/10.1002/aic.690180643`.

Hoppel, W. A., Twomey, S. and Wojciechowski, T. A. (1979), 'A segmented thermal diffusion chamber for continuous measurements of cn', *Aerosol Science* **10**(4), 369–373. DOI: `https://doi.org/10.1016/0021-8502(79)90031-4`.

Jonsson, H., Wilson, J. C., A.Brock, C., Dye, J., Ferry, G. and Chan, K. (1996)), 'Evolution of the stratospheric aerosol in the northern hemisphere following the june 1991 volcanic eruption of mount pinatubo: Role of tropospheric-stratospheric exchange and transport', *J. Geophys. Res.* **101**(D1), 1553–1570. DOI: `http://hdl.handle.net/10945/42241`.

Kangasluoma, J., Ahonen, L., Attoui, M., Vuollekoski, H., Kulmala, M. and Petäjä, T. (2015), 'Sub-3 nm particle detection with commercial tsi 3772 and airmodus a20 fine condensation particle counters', *Aerosol Sci. Tech.* **49**(8), 674–681. DOI: `https://doi.org/10.1080/02786826.2015.1058481`.

Kangasluoma1, J., Kuang, C., Wimmer, D., Rissanen, M. P., Lehtipalo, K., Ehn, M., Worsnop, D. R., Wang, J., Kulmala, M., and Petäjä, T. (2014), 'Sub-3 nm particle size and composition dependent response of a nano-cpc battery', *Atmos. Meas. Tech.* **7**, 689–700. DOI: `https://doi.org/10.5194/amt-7-689-2014`.

Kesten, J., Reineking, A. and Porstendörfer, J. (1991), 'Calibration of a tsi model 3025 ultrafine condensation nucleus counter', *Aerosol Sci. Tech.* **15**(2), 107–111. DOI: `https://doi.org/10.1080/02786829108959517`.

Kousaka, Y., Niida, T., Okuyama, K. and Tanaka, H. (1982), 'Development of a mixing type condensation nucleus counter', *Aerosol Science* **13**(3), 231–240. DOI: `https://doi.org/10.1016/0021-8502(82)90064-7`.

Kuang, C., Chen, M., McMurry, P. H. and Wang, J. (2012), 'Modification of laminar flow ultrafine condensation particle counters for the enhanced detection of 1 nm condensation nuclei', *Aerosol Sci. Tech.* **46**(3), 309–315. DOI: `https://doi.org/10.1080/02786826.2011.626815`.

Kulkarni, P., Baron, P. A. and Willeke, K. (2011), *AEROSOL MEASUREMENT - Priciple, Techniques, and Applications, Third Edition*, Canada: John Wiley and Sons, Inc.

Kupc, A., Bischof, O., Tritscher, T., Beeston, M., Krinke, T. and Wagner, P. E. (2013), 'Laboratory characterization of a new nano-water-based cpc 3788 and performance comparison to an ultrafine butanol-based cpc 3776', *Aerosol Sci. Tech.* **47**(2), 183–191. DOI: `https://doi.org/10.1080/02786826.2012.738317`.

Kutin, J. and Bajsic, I. (2014), 'Fluid-dynamic loading of pipes conveying fluid with a laminar mean-flow velocity profile', *Journal of Fluids and Structures* **50**, 171–183. DOI: `https://doi.org/10.1016/j.jfluidstructs.2014.05.014`.

Köberl, G. (2019), Generation of aerosol nanoparticles of different composition in air and helium, Master's thesis, University of Vienna.

Köhler, H. (1936), 'The nucleus in and the growth of hygroscopic droplets', *Transactions of the Faraday Society* **32**.

Langtangen, H. P. and Logg, A. (2016), *Solving PDEs in Python*, Cham: Springer. DOI: `https://doi.org/10.1007/978-3-319-52462-7`.

Lapuerta, M., Hernandez, J. P. and Agudelo, J. R. (2014), 'An equation for the estimation of alcohol-air diffusion coefficients for modelling evaporation losses in fuel systems', *Applied Thermal Engineering* **73**, 539–548. DOI: `http://dx.doi.org/10.1016/j.applthermaleng.2014.08.009`.

Liao, B.-X., Tseng, N.-C. and Tsai, C.-J. (2018), 'The accuracy of the aerosol particle mass analyzer for nanoparticle classification', *Aerosol Sci. Tech.* **52**(1), 9–29. DOI: `https://doi.org/10.1080/02786826.2017.1370532`.

Liao, H., Chen, W. and Seinfeld, J. H. (2006), 'Role of climate change in global predictions of future tropospheric ozone and aerosols', *J. Geophys. Res.* **111**(D12304). DOI: `https://doi.org/10.1029/2005JD006852`.

McMurry, P. H. (2000), 'The history of condensation nucleus counters', *Aerosol Sci. Tech.* **33**(4), 297–322. DOI: `https://doi.org/10.1080/02786820050121512`.

Mertes, S., Schröder, F. and Wiedensohler, A. (1995), 'The particle detection efficiency curve of the tsi-3010 cpc as a function of the temperature difference between saturator and condenser', *Aerosol Sci. Tech.* **23**(2), 257–261. DOI: `https://doi.org/10.1080/02786829508965310`.

Mordasand, G., Sipilä, M. and Kulmala, M. (2007), 'Nanoparticle Detection Using Nucleation Regime of the CPC', *Nucleation and Atmospheric Aerosols* pp. 209–213. DOI: `https://doi.org/10.1007/978-1-4020-6475-3_43`.

Murphy, D. M., Froyd, K. D., Bian, H., Brock, C. A., Dibb, J. E., DiGangi, J. P., Diskin, G., Dollner, M., Kupc, A., Scheuer, E. M., Schill, G. P., Weinzierl, B., Williamson, C. J. and Yu, P. (2019), 'The distribution of sea-salt aerosol in the global troposphere', *Chem. Phys.* **19**(6), 4093–4104. DOI: `https://doi.org/10.5194/acp-19-4093-2019`.

Petters, M. D. and Kreidenweis, S. M. (2007), 'A single parameter representation of hygroscopic growth and cloud condensation nucleus activity', *Atmos. Chem. Phys.* **7**(8), 1961–1971.

Petters, M. D. and Kreidenweis, S. M. (2008), 'A single parameter representation of hygroscopic growth and cloud condensation nucleus activity – part 2: Including solubility', *Atmos. Chem. Phys.* **8**(20), 6273–6279.

Petters, M. D. and Kreidenweis, S. M. (2013), 'A single parameter representation of hygroscopic growth and cloud condensation nucleus activity – part 3: Including surfactant partitioning', *Atmos. Chem. Phys.* **13**(2), 6273–6279. DOI: `http://dx.doi.org/10.5194/acp-13-1081-2013`.

Pihlava, K., Keskinen, J. and Yli-Ojanperä, J. (2016), 'Improving the signal-to-noise ratio of faraday cup aerosol electrometer based aerosol instrument calibrations', *Aerosol Sci. Tech.* **50**(4), 373–379. DOI: `https://doi.org/10.1080/02786826.2016.1153035`.

Potter, M. C., Hondzo, M. and Wiggert, D. C. (2010), *Mechanics of fluids*, Stamford, CT; Mexico: Cengage Learning.

Ravishankara, A. R. (1997), 'Heterogeneous and multiphase chemistry in the troposphere', *Science* **276**(5315), 1058–1065. DOI: `https://doi.org/10.1126/science.276.5315.1058`.

Reischl, G. P., Mäkelä, J. M., Karch, R. and Necid, J. (1996), 'Bipolar charging of ultrafine particles in the size range below 10 nm', *Aerosol Science* **27**(6), 931–949. DOI: `https://doi.org/10.1016/0021-8502(96)00026-2`.

Rosen, J. M., Pinnick, R. G. and Hall, R. (1974), Proceedings 3rd conference climatic impact assessment program, *in* 'Recent Measurements of Condensation Nuclei in the Stratosphere', Department of Transportation, Washington, D.C.

Scheibel, H. and Porstendörfer, J. (1983), 'Generation of monodisperse ag- and nacl-aerosols with particle diameters between 2 and 300 nm', *Aerosol Science* **14**(2), 113–126. DOI: `https://doi.org/10.1016/0021-8502(83)90035-6`.

Schröder, F. and Ström, J. (1997), 'Aircraft measurements of sub micrometer aerosol particles (> 7 nm) in the midlatitude free troposphere and tropopause region', *Atmos. Res.* **44**, 333–356. DOI: `https://doi.org/10.1016/S0169-8095(96)00034-8`.

Seinfeld, J. H. and Pandis, S. N. (2006), *Atmospheric Chemistry and Physics: from Air Pollution to Climate Change, Second Edition*, New York: John Wiley and Sons, Inc.

Sinclair, D. and Hoopes, G. S. (1975), 'A continuous flow condensation nucleus counter', *Aerosol Science* **6**(1), 1–7. DOI: `https://doi.org/10.1016/0021-8502(75)90036-1`.

Stabile, L., Trassierra, C. V., Dell'Agli, G. and Buonanno, G. (2013), 'Ultrafine particle generation through atomization technique: The influence of the solution', *Aerosol Air Qual. Res.* **13**(6), 1667–1677. DOI: `https://doi.org/10.4209/aaqr.2013.03.0085`.

Steiner, G. (2011), High resolution mobility spectrometry of molecular ions and their effect on the charging probabilities of airborne particles under bipolar diffusion charging conditions, PhD thesis, University of Vienna.

Stolzenburg, M. R. and McMurry, P. H. (1991), 'An ultrafine aerosol condensation nucleus counter', *Aerosol Sci. Tech.* **14**(1), 48–65. DOI: `https://doi.org/10.1080/02786829108959470`.

Takegawa, N. and Sakurai, H. (2011), 'Laboratory evaluation of a tsi condensation particle counter (model 3771) under airborne measurement conditions', *Aerosol Sci Tech* **45**(2), 272–283. DOI: `https://doi.org/10.1080/02786826.2010.532839`.

Tauber, C., Brilken, S., Wlasits, P. J., Bauer, P. S., Köberl, G., Steiner, G. and Winkler, P. (2019), 'Humidity effects on the detection of soluble and insoluble nanoparticles in butanol operated condensation particle counters', *Atmos. Meas. Tech.* **12**(7), 3659–3671. DOI: `https://amt.copernicus.org/articles/12/3659/2019/`.

Tauber, C., Steiner, G. and Winkler, P. M. (2019), 'Counting efficiency determination from quantitative intercomparison between expansion and laminar flow type condensation particle counter', *Aerosol Sci. Tech.* **53**(3), 344–354. DOI: `https://doi.org/10.1080/02786826.2019.1568382`.

TSI Incorporated (2006), *Model 3068B Aerosol Electrometer – User's Manual.* User Manual.

TSI Incorporated (2007), *Model 3772/3771 Condensation Particle Counter – Operation and Service Manual.* User Manual.

TSI Incorporated (2010), 'Advanced Aerosol Neutralizer model 3088', `https://tsi.com/getmedia/d3b50b23-2e1f-4c9f-84e0-76ace485b557/Aerosol%20Neutralizers%203088_US_5001285_RevE_Web?ext=.pdf`. Spec sheet, called on Feb. 11. 2020.

TSI Incorporated (2015), *Condensation Particle Counter Model 3750 – Operation Manual.* User Manual.

TSI Incorporated (2016), 'Condensation particle counter model 3772-CEN', `https://www.tsi.com/getmedia/e6123b1e-3366-429d-a885-8acefc59f801/3772-CEN%20CPC_A4_5001721_Web?ext=.pdf`. Spec sheet, called on Feb. 12. 2020.

TSI Incorporated (2018), 'Condensation particle counter model 3750', `http://tsi.com/getmedia/1f8210ad-7614-4aa1-ac0c-09f4c3bc13fe/3750_A4_5002012_RevB_Web?ext=.pdf`. Spec sheet, called on Feb. 11. 2019.

Vanhanen, J., Mikkilä, J., Lehtipalo, K., Sipilä, M., Manninen, H. E., Siivola, E., Petäjä, T. and Kulmala, M. (2011), 'Particle size magnifier for nano-cn detection', *Aerosol Sci. Tech.* **45**(4), 533–542. DOI: `https://doi.org/10.1080/02786826.2010.547889`.

Wang, Z., Qin, F. and Luo, X. (2018), 'Numerical investigation of effects of curvature and wettability of particles on heterogeneous condensation', *Chem. Phys.* **149**(134306). DOI: `https://doi.org/10.1063/1.5040878`.

Weiden, S.-L. V. D., Drewnick, F. and Borrmann, S. (2009), 'Particle loss calculator – a new software tool for the assessment of the performance of aerosol inlet systems', *Atmos. Meas. Tech.* **2**, 479–494. DOI: `https://doi.org/10.5194/amt-2-479-2009`.

Weinzierl, B., Ansmann, A., Prospero, J. M., Althausen, D., Benker, N., Chouza, F., Dollner, M., Farrell, D., Fomba, W. K., Freudenthaler, V., Gasteiger, J., Groß, S., Haarig, M., Heinold, B., Kandler, K., Kristensen, T. B., Mayol-Bracero, O. L., Müller, T., Reitebuch, O., Sauer, D., Schäfler, A., Schepanski, K., Spanu, A., Tegen, I., Toledano, C. and Walser, A. (2017), 'The saharan aerosol long-range transport and aerosol–cloud-interaction experiment: Overview and selected highlights', *Bull. Amer. Meteor. Soc.* **98**(7), 1427–1451. DOI: `https://doi.org/10.1175/BAMS-D-15-00142.1`.

Wiedensohlet, A., Orsini, D., Covert, D. S., Coffmann, D., Cantrell, W., Havlicek, M., Brechtel, F. J., Russell, L. M., Weber, R. J., Gras, J., Hudson, J. G. and Litchy, M. (1997)), 'Intercomparison study of the size-dependent counting efficiency of 26 condensation particle counters', *Aerosol Sci. Tech.* **27**(2), 224–242. DOI: `https://doi.org/10.1080/02786829708965469`.

Williamson, C., Kupc, A., Wilson, J., Gesler, D. W., Reeves, J. M., Erdesz, F., McLaughlin, R. and Brock, C. A. (2018), 'Fast time response measurements of particle size distributions in the 3–60nm size range with the nucleation mode aerosol size spectrometer', *Atmos. Meas. Tech.* **11**, 3491–3509. DOI: `https://doi.org/10.5194/amt-11-3491-2018`.

Winkler, P. M., Steiner, G., Vrtala, A., Hanna Vehkamäk and, M. N., Lehtinen, K. E. J., Reischl, G. P., Wagner, P. E. and Kulmala, M. (2008), 'Heterogeneous nucleation experiments bridging the scale from molecular ion clusters to nanoparticles', *Science* **319**(5868), 1374–1377. DOI: `10.1126/science.1149034`.

Winklmayr, W., Reischl, G. P., Lindner, A. O. and Berner, A. (1991), 'A new electromobility spectrometer for the measurement of aerosol size distributions in the size range from 1 to 1000 nm', *Aerosol Science* **22**(3), 289–296. DOI: `https://doi.org/10.1016/S0021-8502(05)80007-2`.

Wlasits, P. J., Stolzenburg, D., Tauber, C., Brilke, S., Schmitt, S. H., Winkler, P. M. and Wimmer, D. (2020), 'Counting on chemistry: Laboratory evaluation of seed material-dependent detection efficiencies of ultrafine condensation particle counters', *Atmos. Meas. Tech. Discuss.* . DOI: `https://doi.org/10.5194/amt-2019-486`, in review.

Yang, Y., Yu, T., Zhang, J., Wang, J., Wang, W., Gui, H. and Liu., J. (2018), 'On the performance of an aerosol electrometer with enhanced detection limit', *Sensors* **18**(11). DOI: `https://doi.org/10.3390/s18113889`.

Zhang, Z. and Liu, B. Y. H. (1990), 'Dependence of the performance of tsi 3020 condensation nucleus counter on pressure, flow rate, and temperature', *Aerosol Sci. Tech.* **13**(4), 493–504. DOI: `https://doi.org/10.1080/02786829008959464`.

Zhang, Z. and Liu, B. Y. H. (1991), 'Performance of tsi 3760 condensation nuclei counter at reduced pressures and flow rates', *Aerosol Sci. Tech.* **15**(4), 228–238. DOI: `https://doi.org/10.1080/02786829108959530`.

List of Figures

64

List of Tables

A   Appendix – CPC Performance Tests without n-butanol Fill Bottles

For low pressure measurements, the n-butanol fill bottles were disconnected from the CPCs and the feature 'autofill' was deactivated to avoid flooding of the instruments (for a maximum of three hours). To make sure, that the CPCs still reliably detect particle number concentration without n-butanol replenishment, comparison measurements were carried out at ambient pressure. The results for CPC 1 operated without fill bottle and CPC 2 as reference can be seen in Figure A.1. Figure A.2 shows the measurements where CPC 2 was run without n-butanol replenishment and CPC 1 was used as reference. Measurements were performed at atmospheric pressure for almost 16 hours each. Particle number concentrations were kept high (between about 3000 and 17 000 particles per cubic centimeter) by utilizing PSL (polystyrene latex beads, manufactured by Thermo Scientific (Waltham, Massachusetts)) and an atomizer to generate aerosol particles. This generation method was chosen, since it can be run without thorough, continuous attention. The generation setup was similar to the one described by Stabile et al. (2013). A solution of 60 ± 4 nm PSL in filtered water was nebulized in an atomizer (see Figure 1 in Stabile et al. (2013)) with clean, dry, pressurized air (flow rate of 1.5 l/min). The aerosol was subsequently passed through a silica gel dryer and diluted with clean, dry air (1.5 l/min flow rate), before the flow was split and directed into the CPCs. An exhaust for excessive flow was placed in front of the flow splitter.

As can be seen in Figure A.1 and Figure A.2, both CPCs performances seem to be unaffected by the lack of n-butanol replenishment for the course of 16 hours. Within this time period, no decrease in detection efficiency for the CPCs operated without n-butanol fill bottles, relative to the respective reference instrument, was observed (the fraction of measured particle number concentrations measured by CPC 1 and CPC 2 was approximately 1 with a standard deviation below 1 %). Takegawa and Sakurai (2011) also observed constant detection efficiencies for several hours of measurement time, with the feature 'autofill' turned of, for the TSI 3771 CPC.
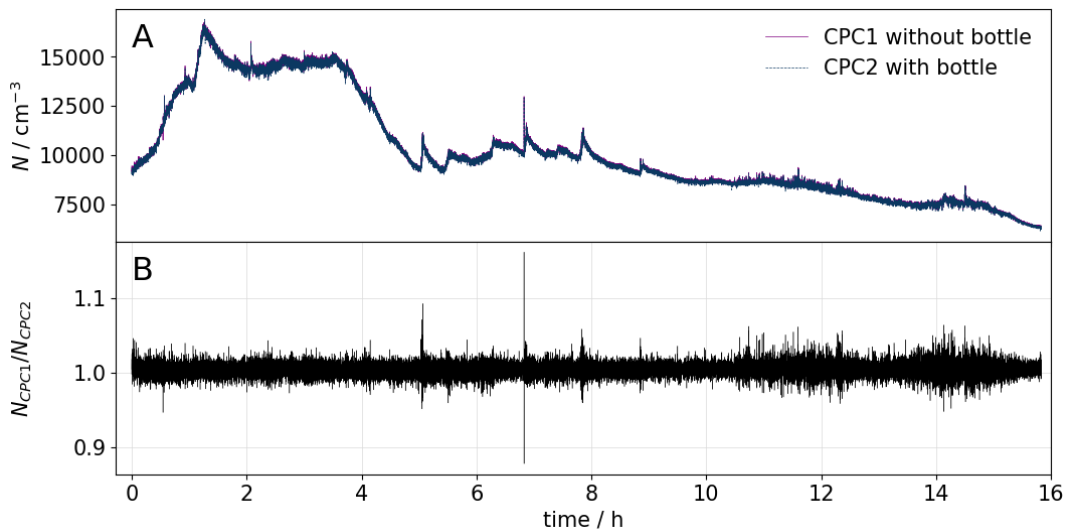

Figure A.1: Performance test with CPC 1 disconnected from its fill bottle, using CPC 2 as reference. For 60 nm PSL particles generated by an atomizer. Plot A shows the measured concentrations of both CPCs, plot B the relation between the detected particle number concentrations of CPC 1 and CPC 2.

Figure A.2: Performance test with CPC 2 disconnected from its fill bottle, using CPC 1 as reference. For 60 nm PSL particles generated by an atomizer. Plot A shows the measured concentrations of both CPCs, plot B the relation between the detected particle number concentrations of CPC 1 and CPC 2.
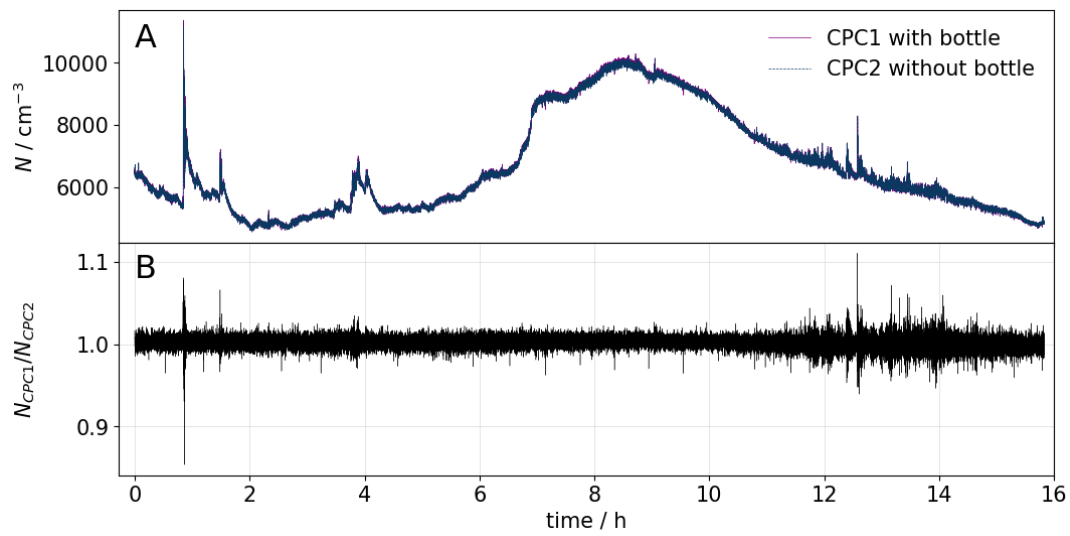
B Appendix Pressure dependent Detection Efficiency for Silver Particles

Figure B.1 depicts the pressure dependent detection efficiency measurement results for all measured silver particle diameters and both CPCs. In Figure B.1, also the second 7 nm curve with open markers is included. For the measurement of this curve, the detection setup had to be readjusted to room pressure twice due to flow problems, which could possibly have influenced the results.
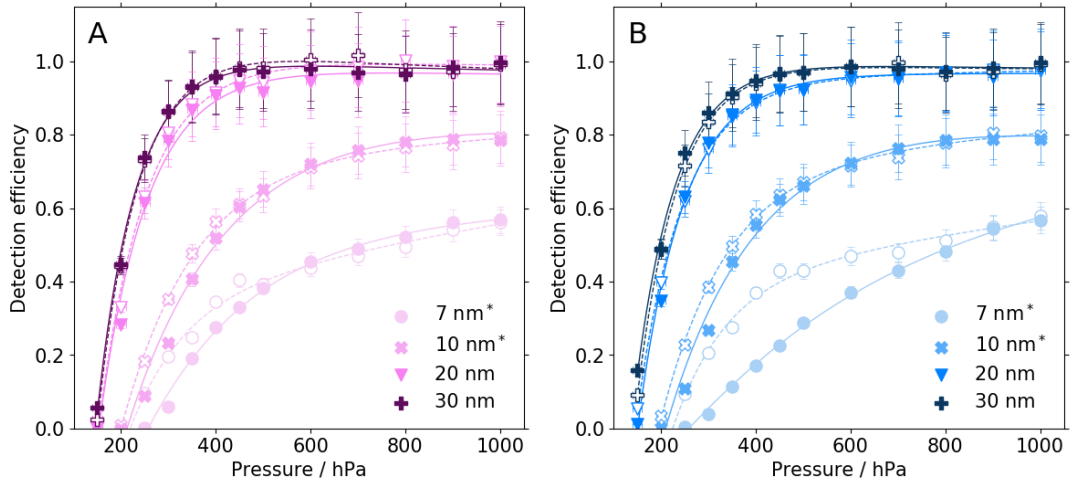

Figure B.1: Pressure dependent detection efficiency curves of two measurement cycles, recorded on different days (markers filled and not filled respectively) for silver particles, with diameters D_p ranging from 7 nm to 30 nm. For CPC 1 (A) and CPC 2 (B). *Since only a fraction of 7 (close to cutoff size) and 10 nm particles are detected already at pressure of 1000 hPa (60 and 80 % efficiency respectively), the detection efficiency curves for these two particle sizes lie below curves for bigger particle sizes (i.e. 20 and 30 nm). This indicates that when particles are below 100 % detection of a CPC at 1000 hPa (ground level pressure) two effects come into place: the effect of particle size and pressure (in contrast to bigger sizes, where pressure is the most important factor).

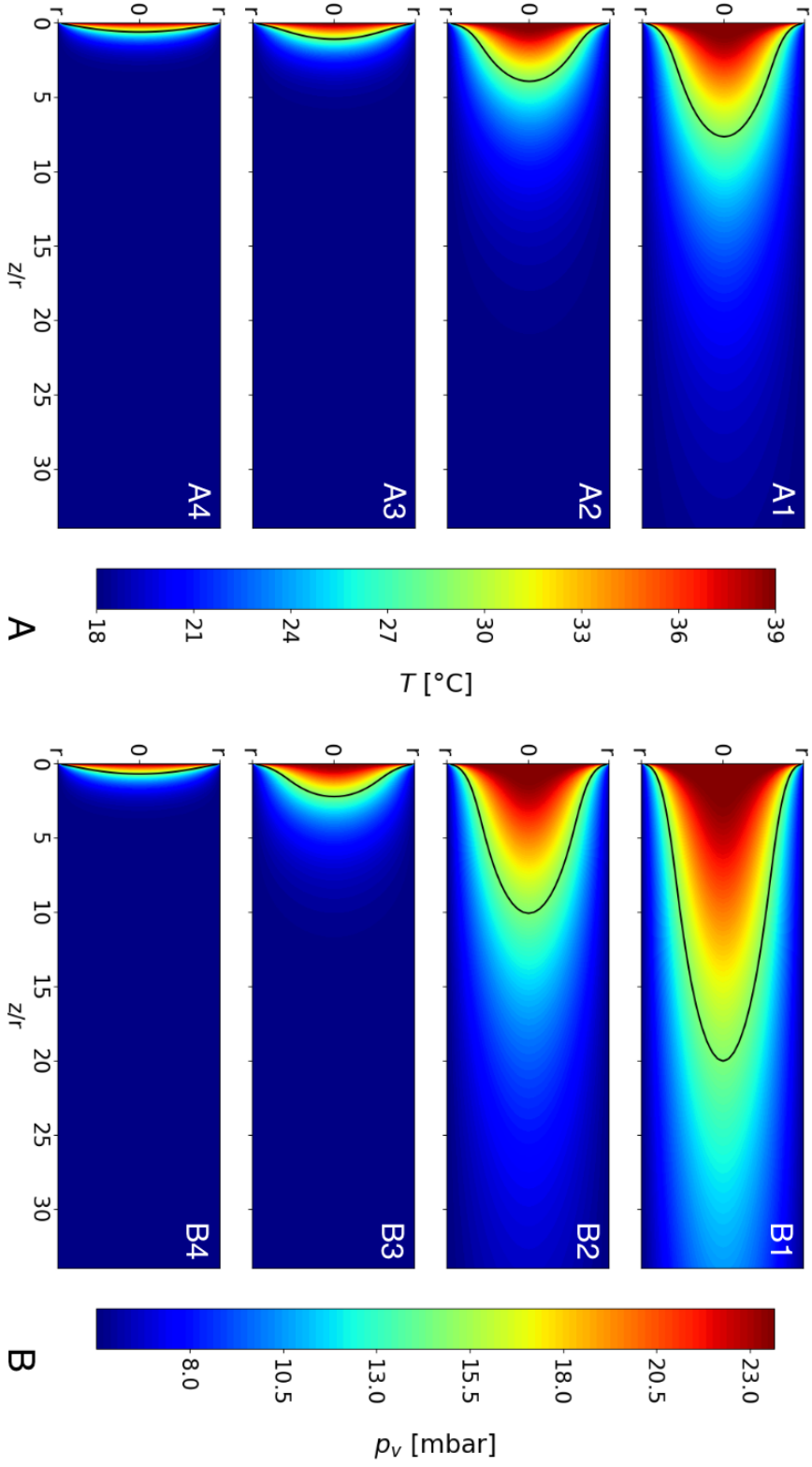# C Appendix – TSI 3772-CEN Condenser Profiles

Figure C.1: Simulated temperature (A) and partial vapor pressure (B) profiles inside the condenser tube of the TSI 3772-CEN at 1000 hPa (A1,B1), 500 hPa (A2,B2), 100 hPa (A3,B3), 10 hPa (A4,B4) ambient pressure. With the radius r and the dimensionless length z/r of the tube. The color coding shows the temperature and partial vapor pressure distribution. The black lines show areas with a temperature of 28.5 °C (A) or partial vapor pressure of 14.6 mbar (B).

D   Appendix – TSI 3772-CEN Silver Particle Cutoffs at various Condenser Temperature Settings

It has been shown before, that the cutoff diameter of a n-butanol based CPC can be altered, by changing the temperature difference ΔT between saturator and condenser (see Mertes et al. (1995)). A larger ΔT leads to a smaller D_{50}, a smaller ΔT to a larger D_{50}. Figure D.1 displays the experimental and theoretical cutoff curves for silver particles at ambient pressure, for the TSI 3772-CEN CPC and two condenser temperature settings. Here ΔT_{medium} (yellow markers and lines) refers to the manufacturer settings, described in paragraph 3.1.3.1, for ΔT_{high} (grey markers and lines) the condenser temperature was reduced from 18 °C to 10 °C. It was made sure, that no homogeneous nucleation occurred at the altered temperature settings, by placing a HEPA filter in front of the CPC. In the configuration with the filter, the CPC did not detect any particles. Also included in Figure D.1 are data points taken from Wlasits et al. (2020) for silver particles and the TSI 3772 CPC, in which the condenser temperature is set to 22 °C (black data points, ΔT_{low}). The black dashed line, depicts the corresponding theoretical cutoff curve. All cutoff values are listed in Table D.1.

Table D.1: Experimental and theoretical cutoff values, for varying temperature differences between saturator and condenser. $D_{50,low}$ corresponds to $\Delta T = 17$ °C (taken from Wlasits et al. (2020)), $D_{50,medium}$ to $\Delta T = 21$ °C and $D_{50,high}$ to $\Delta T = 29$ °C respectively.

	$D_{50,low}$ [nm]	$D_{50,medium}$ [nm]	$D_{50,high}$ [nm]
Experimental	8.8 ± 1.0	6.4 ± 0.8	4.1 ± 0.5
Simulation	9.5	7	4.3

A good agreement between measurement data and simulation data was found for all three temperature settings.
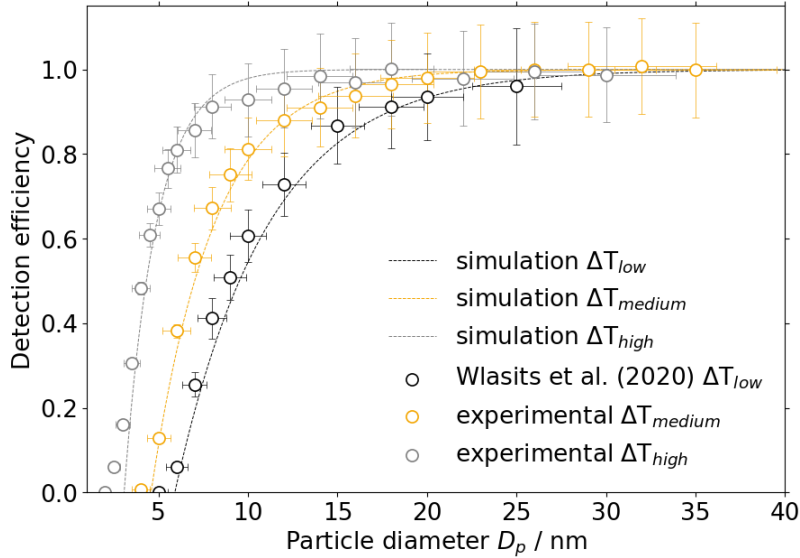

Figure D.1: Silver particle cutoff curves for three different condenser temperature settings, respectively changing ΔT between saturator and condenser. The data points are experimental results, the lines are the respective theoretical detection efficiencies. ΔT_{low} corresponds to $\Delta T = 17$ °C (experimental data taken from Wlasits et al. (2020)), ΔT_{medium} to $\Delta T = 21$ °C and ΔT_{high} to $\Delta T = 29$ °C respectively.